PLEASE CITE THIS ARTICLE AS DOI: 10.1063/5.0093083

Journal of Applied Physics

AIP Publishing

Understanding the role of resonances and anti-resonances in shaping surface-wave bandgaps for metasurfaces

Lalith Sai Srinivas Pillarisetti,[1] Cliff J Lissenden,[1] and Parisa Shokouhi[1, a)]

Department of Engineering Science and Mechanics, Penn State, University Park, Pennsylvania 16802, USA

(Dated: 20 September 2022)

An array of surface-mounted prismatic resonators in the path of Rayleigh wave propagation generates two distinct types of surface-wave bandgaps: longitudinal and flexural-resonance bandgaps, resulting from the hybridization of the Rayleigh wave with the longitudinal and flexural resonances of the resonators, respectively. Longitudinal-resonance bandgaps are broad with asymmetric transmission drops, whereas flexural-resonance bandgaps are narrow with nearly symmetric transmission drops. In this paper, we illuminate these observations by investigating the resonances and anti-resonances of the resonator. With an understanding of how the Rayleigh wave interacts with different boundary conditions, we investigate the clamping conditions imposed by prismatic resonators due to the resonator's resonances and anti-resonances and interpret the resulting transmission spectra. We demonstrate that, in case of a single resonator, only the resonator's longitudinal and flexural resonances are responsible for suppressing Rayleigh waves. In contrast, for a resonator array, both the resonances and the anti-resonances of the resonators contribute to the formation of the longitudinal-resonance bandgaps, unlike the flexural-resonance bandgaps where only the flexural resonances play a role. We also provide an explanation for the observed asymmetry in the transmission drop within the longitudinal-resonance bandgaps by assessing the clamping conditions imposed by the resonators. Finally, we evaluate the transmission characteristics of resonator arrays at the anti-resonance frequencies by varying a few key geometric parameters of the unit cell. These findings provide the conceptual understanding required to design optimized resonators based on matching anti-resonance frequencies with the incident Rayleigh wave frequency in order to achieve enhanced Rayleigh wave suppression.

[a)] parisa@psu.edu

Journal of Applied Physics

AIP Publishing

I. INTRODUCTION

In the past two decades, numerous investigations have shown how to control surface waves using locally resonant metamaterials. These metamaterials comprise an array of resonators that exhibit bandgaps resulting from the hybridization of the incident wave with the local resonances of the resonators[1–3]. There have been meta-barrier configurations with near-surface buried spring-mass resonators[4,5], and meta-surface configurations comprising surface-mounted prismatic resonators to suppress surface wave propagation[6–10]. The former configuration yields bandgaps at the resonance frequencies of the spring-mass resonators, whereas the latter configuration yields bandgaps at the longitudinal and flexural resonances of the resonators. The state-of-the-art metasurface design is based on matching the longitudinal resonance frequency of the resonators with the incident wave frequency, limiting the systematic designs to mostly prismatic rod-like resonators.

Very recently, Hakoda *et al.* proposed a nonintuitive four-arm resonator design to suppress the incident S0 Lamb wave mode in a plate[11]. This design is based on matching the anti-resonance frequency (corresponding to the horizontal displacement U_1) of the resonator with the incident S0 Lamb wave frequency[12]. Anti-resonance frequencies of the resonator represent the frequencies at which a near-zero displacement (either horizontal (U_1) or vertical (U_3)) at the resonator's base is achieved due to the dynamics of the system. It was demonstrated that obtaining the U_1 displacement anti-resonance for a resonator subjected to a horizontal harmonic traction loading at the resonator base is sufficient to suppress the S0 wave at the corresponding anti-resonance frequency[12]. Similarly, obtaining the U_3 displacement anti-resonance for a resonator subjected to vertical harmonic traction loading is sufficient for suppressing the A0 wave[12,13]. The predominant U_1 particle motion of the S0 wave and U_3 particle motion of the A0 wave at low frequencies could be a possible explanation for these observations. However, unlike the Lamb wave modes A0 and S0, the surface wave particle motion has displacement components in both the horizontal and vertical directions (Fig. 1(a)), suggesting the need for a more robust analysis to realize anti-resonance frequency-matching design strategies for surface wave control.

Earlier studies of metasurfaces with rod-like resonators show the existence of anti-resonance frequencies (f_A) for plate waves[11–14] and surface waves[9,15,16] near the bandgap frequencies. For ease of discussion, we use the terms "longitudinal resonance bandgap"

Journal of Applied Physics

AIP Publishing

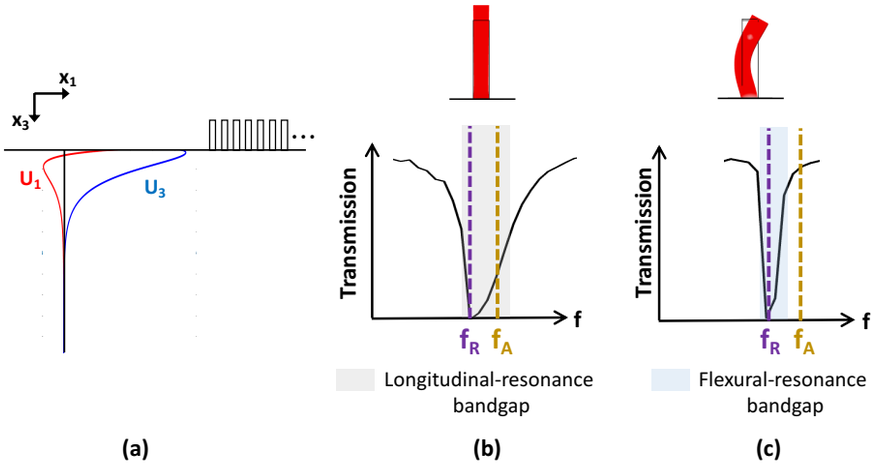

FIG. 1. (a) Schematic of the Rayleigh wave incidence on an array of surface-mounted rod-like resonators and the surface-wave bandgaps obtained because of the (b) longitudinal and (c) flexural resonances of the resonator. The resonance (f_R) and anti-resonance (f_A) frequencies of the resonator corresponding to the longitudinal-resonance and flexural-resonance bandgaps are schematically marked for reference.

and "flexural resonance bandgap" to refer to surface-wave bandgaps associated with resonator's longitudinal and flexural resonances, respectively (Figs. 1(b) and 1(c)). Colombi *et al.* demonstrated that the onset of the longitudinal resonance surface-wave bandgap coincides with the coupled longitudinal resonance frequency (f_R) of the resonator and the bandgap ends at the anti-resonance frequencies (Fig. 1(b))[9]. It is worth noting that the anti-resonance frequencies are generally different from the coupled resonance frequencies of the resonators, which represent the frequencies of maximum displacement response, evaluated by taking into account the frequency shift due to the stiffness contribution of the half-space[17]. For a rigid half-space, the coupled resonance frequency is the same as its corresponding anti-resonance frequency. The coincidence of the longitudinal resonance bandgap's beginning with the resonator's longitudinal resonance frequency (Fig. 1(b)) is attributed to the hybridization between the incident Rayleigh wave and the longitudinal resonance of the resonator that results in a π phase shift of the incident wave[17].

Very recently, Pu *et al.* presented an analytical formulation based on multiple scattering theory to determine the coupled resonance frequencies for mass-spring resonators in the path of Rayleigh wave propagation[17]. These resonance frequencies are demonstrated to be

dependent on the resonator mass, spring stiffness, and the equivalent frequency-dependent half-space stiffness and require rigorous analytical derivations to be calculated for different resonator geometries. These resonance frequency considerations were disregarded in the closed-form solution of the surface wave bandgap width evaluated by Colquitt *et al.*[15], where the bandgap between the coupled resonance frequency and the anti-resonance frequency has not been considered. Currently, most of the meta-surface designs for elastic wave control are based on computationally-expensive parametric tuning of the bandgaps using finite element methods, performing eigenfrequency analysis of the unit cell by varying multiple geometric constraints[18–21]. A rational design procedure for resonators to suppress Rayleigh waves by generating bandgap at the desired frequency is lacking. An ideal design methodology should be capable of designing the resonator without the need for coupling it to the half-space, only requiring knowledge of the elastic wave propagation characteristics, desired bandgap frequency range, and resonator material properties.

Rather than dealing with resonances, the resonator design based on tailoring anti-resonances under a dynamic load emulating the incident wave propagation could enable a rational design strategy for designing resonators using topology optimization. In contrast to the resonance frequencies, which decide the lower bound of the bandgap, the anti-resonance frequencies of the resonator are observed to fall within and close to the upper bound of the bandgap for rod-like resonators, as schematically represented in Fig. 1(b)[9]. However, this holds only for the case of anti-resonances of the resonator undergoing longitudinal vibrations but not the flexural vibrations (Fig. 1(c)), as will be demonstrated in this paper. It was numerically demonstrated that imposing a type of Cauchy boundary conditions (BCs), called Mindlin BCs, which is equivalent to having U_3 displacement anti-resonance for a resonator, can effectively suppress Rayleigh wave propagation[16]. This observation can be exploited to design nonintuitive resonators based on anti-resonance matching through topology optimization.

A BC-based design strategy requires an in-depth understanding of the interaction of Rayleigh waves with the clamping boundary conditions imposed by surface-mounted resonators and the role of resonator resonances and anti-resonances (longitudinal and flexural) in tailoring surface-wave bandgaps. A recent study revealed that constraining the horizontal component of displacement (Auld BCs) in the path of Rayleigh wave propagation does not suppress Rayleigh waves; instead, the Rayleigh wave mode transmits as surface propagat-

Journal of Applied Physics

AIP Publishing

ing transverse waves[16]. Therefore, the role of U_1 displacement anti-resonance in creating flexural resonance bandgaps needs to be further investigated. In addition, previous investigations show that local resonance-based bandgaps are asymmetric in shape[9,22], with more transmission drop near the lower bound compared to the upper bound. It is interesting to investigate whether the asymmetry in the transmission spectrum within the bandgap correlates with the BCs imposed by resonators at the resonance and anti-resonance frequencies on the half-space. Finally, it was demonstrated that both the A0 and S0 Lamb waves can be significantly suppressed using only a 1D array of resonators at the resonator's anti-resonance frequency[12], giving rise to the question of whether we can achieve similar control over surface waves. To that end, it is important to analyze separately the influence of clamping conditions imposed by a single resonator and an array of resonators at the resonance and anti-resonance frequencies on the incident Rayleigh wave propagation and investigate its implications on the transmission spectra.

To the best of the authors' knowledge, this is the first study that demonstrates how the longitudinal and flexural resonance bandgaps are shaped in relation to resonances and anti-resonances of surface-mounted prismatic resonators using our understanding of Rayleigh wave interaction with different boundary conditions along its wave propagation path. We draw key conclusions from the behavior of rod-like resonators under Rayleigh wave propagation and hypothesize a rational meta-surface design strategy based on topology optimization. The remainder of the paper is organized as follows. Section II reviews the mode-conversions that result due to the incidence of Rayleigh waves on different surface BCs and provide frequency-domain finite element analyses to understand the interplay between the clamping conditions imposed by resonators and the observed transmission spectra for a single resonator (Section II A) and an array of resonators (Section II B) mounted on the surface in the path of Rayleigh wave propagation. Section III illustrates the influence of few essential geometric parameters on the resonance and anti-resonance frequencies and their integrated effect on the resulting transmission spectra. Finally, we present a set of conclusions in Section IV that motivate and inform possible nonintuitive resonator designs based on anti-resonance-matching using topology optimization.

Journal of Applied Physics

AIP Publishing

II. CLAMPING CONDITIONS IMPOSED BY SURFACE-MOUNTED RESONATORS IN THE PATH OF RAYLEIGH WAVE PROPAGATION

Manipulating the BCs on an elastic half-space was recently shown to achieve control over the Rayleigh wave propagation[16]. An analytical study aimed at finding surface wave solutions for different BCs on an elastic half-space showed that clamping the vertical (U_3) displacement component (termed as Mindlin BCs) on the surface enables Rayleigh wave suppression[16], as the incident Rayleigh wave predominantly mode converts to a transverse wave propagating at an angle into the half-space. Moreover, clamping both the U_1 and U_3 displacement components (Dirichlet BCs) is expected to prevent the propagation of surface waves. On the other hand, constraining the horizontal (U_1) displacement component on the surface of the half-space (termed as Auld BCs) results in possible shear-vertical surface wave solutions and was therefore hypothesized not to play a role in Rayleigh wave suppression[16]. These analytical results can be conceptually understood. Since the shear-vertical waves propagate by pure shear deformation without inducing volume change, they can be supported at the surface even if the horizontal displacement component is constrained (Auld BCs). On the contrary, constraining the vertical displacement component (Mindlin BCs) prevents both the pure shear deformation and the volume change. The lack of pure shear deformation prevents shear-vertical wave propagation, and the constraint on the volume change prevents longitudinal wave propagation on the surface. The time-domain simulations corroborating the above analytical findings are demonstrated in the Supplementary material (See Fig. SM2).

Though imposing frequency-independent BCs is unrealistic, it is possible to impose frequency-dependent Mindlin BCs (or U_3 displacement anti-resonance) and Auld BCs (or U_1 displacement anti-resonance) using surface-mounted resonators at their anti-resonance frequencies, as previously demonstrated for the control of A0 and S0 wave modes in a plate[12] and the control of Rayleigh waves on the half-space[16]. For example, a rod-like resonator constraining the U_3 displacement component at its anti-resonance frequencies is equivalent to imposing Mindlin BCs, whereas constraining the U_1 displacement component is equivalent to imposing Auld BCs. The former scenario is realized when the anti-resonance frequency involves longitudinal vibrations, whereas the latter results if the anti-resonance frequency involves flexural vibrations.

If we are to impose Mindlin BCs in the path of Rayleigh waves by a surface-mounted resonator, it is rational to assume that a single resonator is insufficient to suppress Rayleigh waves at its anti-resonance frequency considering the parametric study on the Mindlin BC patch length illustrated in[16]. For example, to suppress a 500 kHz ($\lambda_R = 5.8$ mm) Rayleigh wave, the required length (L) of the prismatic rod-like resonator should be around 2.5 mm (anti-resonance frequency $\sim$ 500 kHz under Rayleigh wave propagation). Assuming an aspect ratio (L/W) of at least 5 constrains the resonator width (W) to 0.5 mm ($\sim \lambda_R/10$), which is shown to provide minimal Rayleigh wave suppression from the study on frequency-independent Mindlin BC patches[16]. Though a single resonator is expected to exhibit a poor Rayleigh wave suppression, studying its dynamic response and the imposed clamping conditions on the half-space under Rayleigh wave propagation can provide key insights into the anti-resonance-based resonator design methodology, as will be illustrated in the subsequent section.

A. A single surface-mounted resonator

Let us start by analyzing the clamping conditions imposed by a surface-mounted resonator in the path of Rayleigh wave propagation and its corresponding transmission characteristics. For that purpose, we re-visit the COMSOL[23] frequency-domain finite element analysis of a single resonator presented in[16]. The finite element model considered is of thickness (along the x_3 direction) $6\lambda_R$, partitioned into a "buffer" region of length λ_R, "incident" region of length $4\lambda_R$, "resonator" region of length equivalent to the resonator base dimensions, and a "transmitted" region of length $4\lambda_R$, as shown in Fig. 2(a). In a 2D plane strain model of half-space and resonator, the resonator will act as a wall of infinite thickness, and therefore an accurate representation of the resonator's flexural resonances/anti-resonances is not possible. Therefore, a 3D model is required for this analysis. Material properties of Aluminum (Young's modulus = 69 GPa, poisson ratio = 0.33, and density = 2700 kg/m^3) are used for both the half-space and resonators for simulations throughout the paper. Targeting the first fixed-free longitudinal eigenfrequency (fixed-free configuration) around 500 kHz (510 kHz), a 2.5 mm long (L) resonator with a 0.5 mm $\times$ 0.5 mm (W $\times$ W) cross-sectional area (aspect ratio, L/W = 5) is considered. The width of half-space (along the x_2 direction) is considered to be $\lambda_R/4$, where λ_R is the Rayleigh wavelength corresponding to 500 kHz

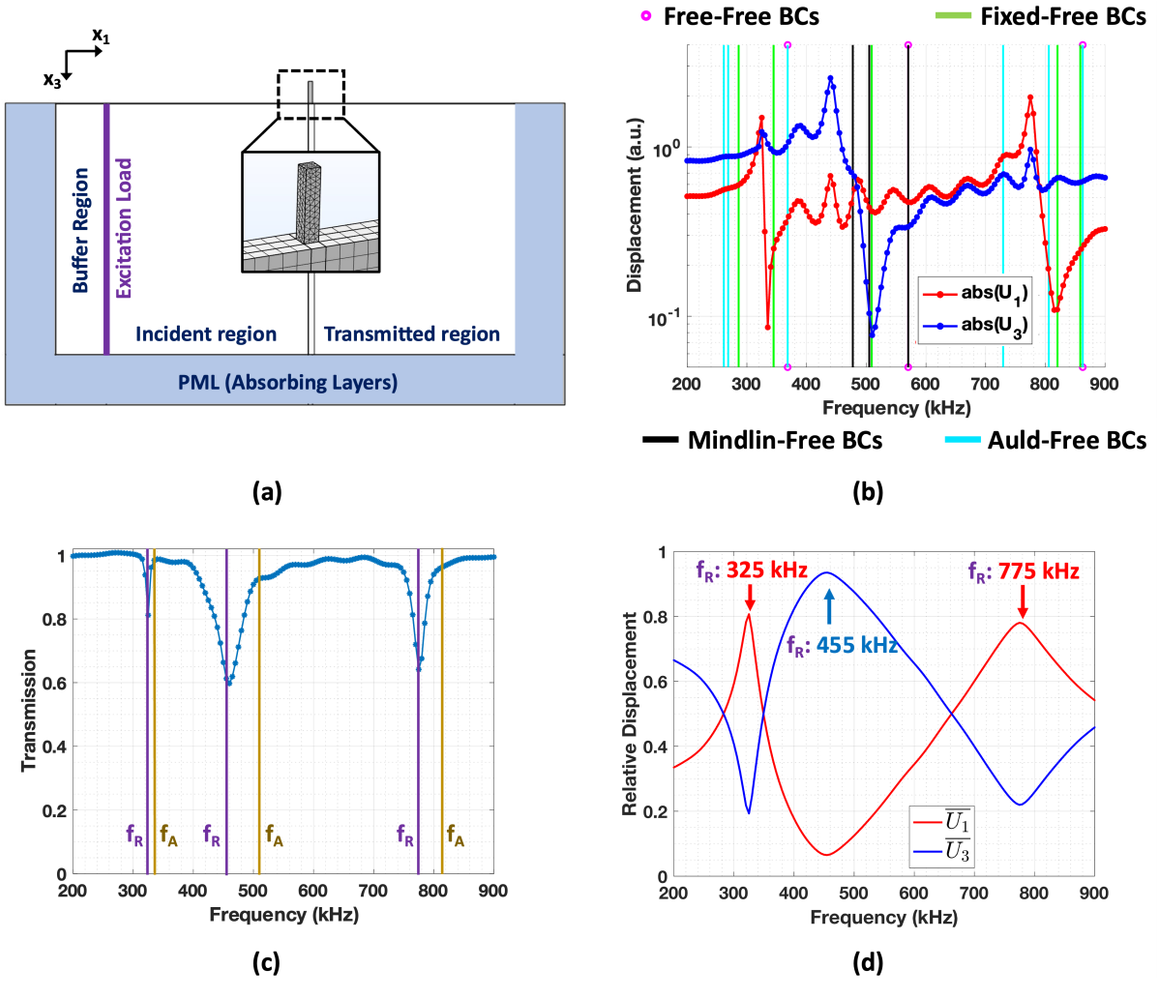

FIG. 2. (a) Schematic of a traction-free elastic half-space with a single resonator surface-mounted on the "resonator" region. (b) Anti-resonance profiles (abs(U_1) and abs(U_3)) of the resonator base, (c) Rayleigh wave transmission spectrum, and (d) Volume averaged relative displacement profiles indicating longitudinal and flexural resonance frequencies for a sweep of Rayleigh wave excitation frequencies. The vertical lines in (c) indicate the resonance (f_R) and anti-resonance (f_A) frequencies of the resonator.

frequency. The periodic BCs are applied to all the lateral surfaces of the half-space to ensure planar wave solutions. The consideration of periodic BCs will assume periodic arrangement of an infinite number of resonators in the x_2 direction, with the width of the half-space dictating the resonator spacing.

A line-load excitation mimicking the wave structure of Rayleigh wave is applied to the left edge of the "incident" region, across the half-space thickness, as shown in Fig. 2 (a).

A cubic mesh size of $\lambda_R/14$ (for the half-space) and a more refined tetrahedral mesh (for the resonator) are used to perform a frequency-domain study by parametric sweeping the excitation frequencies from 200 kHz to 900 kHz in 5 kHz increments. The frequency response (displacement versus frequency) of the resonator to the Rayleigh wave propagation (for determining the exhibited anti-resonances) and the corresponding Rayleigh wave transmission characteristics will be discussed in the subsequent sections.

1. Anti-resonance analysis

The spatially averaged value of the displacements (abs(U_1) and abs(U_3)) over the resonator base, representative of the clamping conditions imposed by the resonator under dynamic loading, plotted for the range of excitation frequencies, is depicted in Fig. 2(b).The eigenfrequencies of the resonator under the free-free, fixed-free, Mindlin-free, and Auld-free BCs applied to the bottom and top resonator surfaces, respectively, are marked for reference. As shown in Fig. 2(b), the U_3 displacement anti-resonance frequency (510 kHz) nearly coincides with the Mindlin-free (505 kHz) and fixed-free (509.1 kHz) eigenfrequencies corresponding to longitudinal vibrations. In other words, the resonator base strictly imposes Mindlin BCs on the half-space at this anti-resonance frequency. In contrast, we observe that the U_1 displacement anti-resonance frequencies (335 kHz and 815 kHz) are not close to the Auld-free eigenfrequencies (261.4 kHz and 729.2 kHz) corresponding to flexural vibrations, suggesting imperfect imposing of Auld BCs. Please note that the cyan line close to 805 kHz does not correspond to the flexural mode. Although the resonator mounted in the path of Rayleigh wave propagation is subjected to vertical and horizontal tractions as well as moments at its base, we further simplify the problem by decoupling the resonator from the half-space to compute the displacement response (U_1 for the horizontal traction loading and U_3 for the vertical traction loading) at the resonator base in the free-free configuration in response to the horizontal and vertical harmonic traction loadings applied to all the nodes of the resonator base (Fig. 3(a)). Obvious dips in the displacement profiles (abs(U_1) and abs(U_3)) can be observed in Fig. 3(a), where the dip in abs(U_3) profile corresponds to the first-mode longitudinal vibrations (Fig. 3(b)), and the dips in abs(U_3) profile correspond to the first (Fig. 3(c)) and second (Fig. 3(d)) mode flexural vibrations.

Drawing a comparison between Figs. 2(b) and 3(a) the U_1 displacement anti-resonance

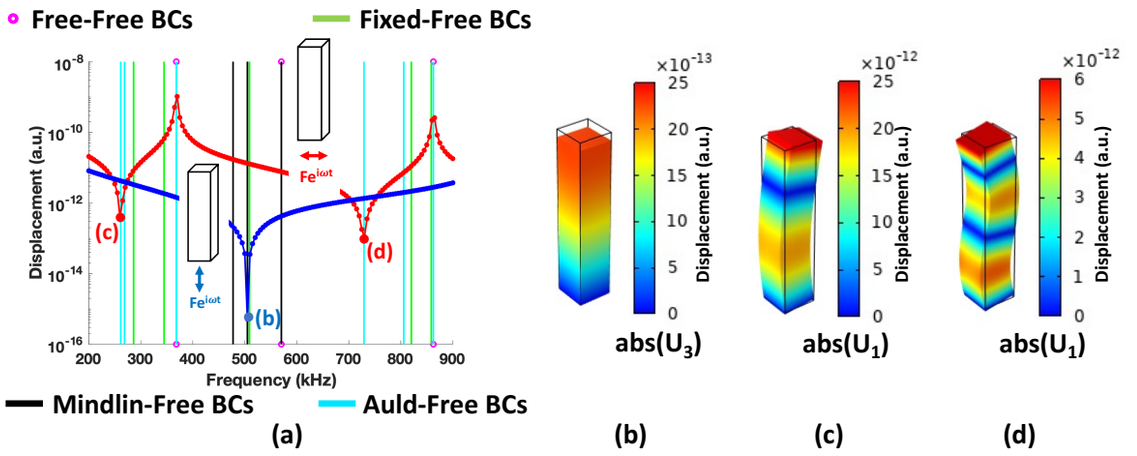

FIG. 3. (a) The displacement response (abs(U_1) for the horizontal traction loading and abs(U_3) for the vertical traction loading) at the resonator base for the vertical and horizontal harmonic forced excitation applied to the resonator base, respectively. The mode shapes of the resonator at the (b) U_3 displacement anti-resonance frequency and the U_1 displacement anti-resonance frequencies corresponding to the (c) first and (d) second flexural modes.

frequencies (335 kHz and 815 kHz) computed for the resonator mounted in the path of Rayleigh wave propagation do not match the U_1 displacement anti-resonance frequencies (260 kHz and 730 kHz) of the same resonator decoupled from the half-space undergoing horizontal forced excitation. This suggests the inability of horizontal harmonic traction loading in emulating a similar anti-resonance behavior to that of a resonator mounted in the path of Rayleigh wave propagation. However, emulating the U_1 displacement anti-resonance frequencies under a simplified loading is not beneficial for Rayleigh wave suppression due to the inefficiency of Auld BCs in suppressing Rayleigh waves (see Supplementary material).

On the other hand, the U_3 displacement anti-resonance frequency computed for the resonator mounted in the path of Rayleigh wave propagation matches well the U_3 displacement anti-resonance frequency of the same resonator decoupled from the half-space under vertical forced excitation, which in turn matches the fixed-free and Mindlin-free eigenfrequencies of the resonator (Figs. 2(b) and 3(a)). In other words, vertical harmonic traction loading applied to a resonator base under free-free configurations can emulate a similar anti-resonance behavior to that of a resonator mounted under Rayleigh wave propagation. These observations motivate a systematic design of resonators based on matching the U_3 displacement

anti-resonance frequency with the incident Rayleigh wave frequency using topology optimization. One of the main benefits of this approach is that it enables designing nonintuitive resonators alleviating the need to couple the resonator to the half-space and using vertical harmonic traction loading.

2. Transmission characteristics

Although anti-resonance matching offers a pathway to systematic resonator design, a single resonator designed based on tailoring its U_3 displacement anti-resonance frequency will have inherent limitations. This is because the transmission characteristics of a Rayleigh wave incident on a finite sized Mindlin BC patch depends on the length of the BC patch[16]. To demonstrate this point, the Rayleigh wave transmission beyond a single resonator is evaluated at each frequency by performing a spatial Fourier transform (SFT) over the complex displacement data ($U_1 + U_3$) extracted along the top surface of the "incident" and "transmitted" regions (Fig. 2(a)). The transmission spectrum shown in Fig. 2(c) is the ratio of the spectral content corresponding to Rayleigh wave peaks in the wavenumber spectra for "transmitted" and "incident" regions plotted versus frequency. We observe three drops in the transmission spectrum at frequencies: 325 kHz, 460 kHz, and 775 kHz. These are the coupled resonance frequencies, i.e., the frequencies at which the resonator exhibits maximum displacement response upon Rayleigh wave incidence. For a resonator in the path of Rayleigh wave propagation, the coupled resonance frequencies (longitudinal and flexural) can be determined by estimating the relative volume-averaged displacements ($\overline{U}_1$ and $\overline{U}_3$) of the resonators for a sweep of Rayleigh wave excitation frequencies:

$$\overline{U}_i = \frac{\sum\sum\sum abs\,(U_i)dV}{\sum\sum\sum\,(abs(U_1) + abs\,(U_3))dV} \quad , \; i \; = \; 1, \; 3. \tag{1}$$

We observe the longitudinal resonance (maximum of $\overline{U}_3$) around 455 kHz and two flexural resonances (maximum of $\overline{U}_1$) at 325 kHz and 775 kHz (Fig. 2(d)). These resonance frequencies have a good correspondence with the frequencies where we observe transmission drops (Fig. 2(c)). On the other contrary, neither the U_3 (imposing Mindlin BCs) nor U_1 (imposing Auld BCs) displacement anti-resonances of the resonator exhibits Rayleigh wave suppression at the anti-resonance frequencies (335 kHz, 510 kHz, and 815 kHz). The latter is expected because U_1 displacement anti-resonances (Auld BCs) do not play a role in

suppressing the Rayleigh wave, whereas the U_3 displacement anti-resonances (Mindlin BCs) require a sufficient width of the resonator base ($\sim 10\lambda_R$) to provide significant suppression[16]. It is worth noting that unlike a coupled resonator in the path of Rayleigh wave propagation, a resonator decoupled from the half-space under vertical or horizontal traction loading at the base will have resonance frequencies coincident with its eigenfrequencies (corresponding to their respective eigenmode) under a free-free configuration, as shown in Fig. 3(a). The above analysis of a single resonator's transmission characteristics showcases a significant limitation of the proposed anti-resonance matching methodology to design resonators, as the anti-resonance (imposing Mindlin BCs) does not readily suppress the Rayleigh wave in comparison to resonance, which is a result of local-resonance hybridization of the resonator with the incident wave[17]. However, a significant Rayleigh wave suppression at the U_3 displacement anti-resonance frequency can be obtained using an array of resonators, as an array of Mindlin BC patches can effectively suppress Rayleigh waves with each patch mode-converting a part of the Rayleigh waves into transverse waves[16].

B. An array of closely spaced surface-mounted resonators

To corroborate the presence of anti-resonances for an array of resonators and their efficiency in suppressing Rayleigh waves, an investigation of the clamping conditions imposed by a resonator array including anti-resonance and transmission analyses is provided in this section.

1. Unit cell dispersion analysis

Before proceeding with the anti-resonance analysis of a resonator array, we present the details of the unit cell dispersion analysis to obtain the surface wave dispersion curves for an infinite 1D array of resonators (in the wave propagation direction) and the corresponding bandgaps following[22]. The unit cell length is considered to be the same as the half-space width ($\lambda_R/4$) used in the earlier investigation resulting in a 2D square lattice configuration for resonators (Fig. 4(a)). The Bloch Floquet periodic BCs are imposed on the four lateral sides of the half-space part of the unit cell, leaving the lateral resonator surfaces traction-free[22]. Fixed BCs are applied to the bottom surface of the half-space to remove

Journal of Applied Physics

AIP Publishing

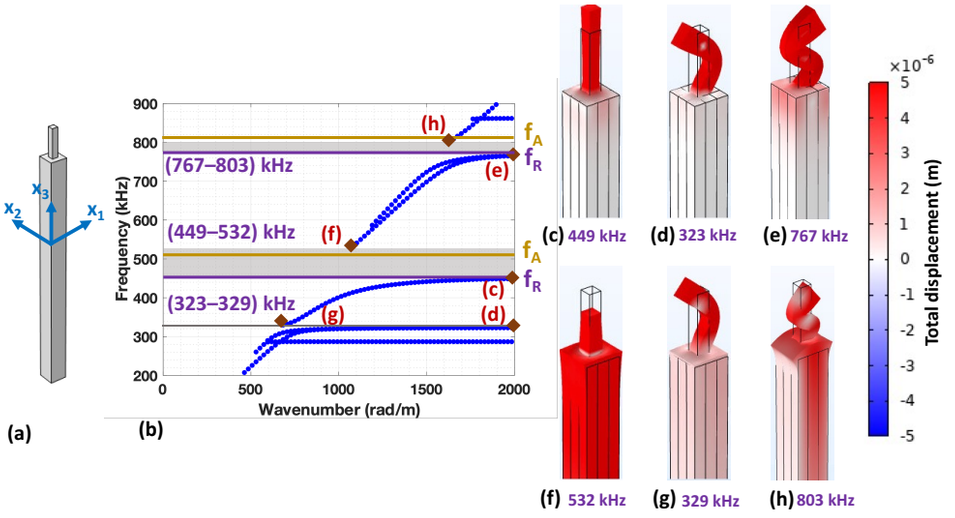

FIG. 4. (a) Unit cell used to compute the (b) surface wave dispersion curves exhibiting three surface-wave bandgaps formed due to a longitudinal resonance and two flexural resonances of the resonator. The mode shape of the resonator-half space unit cell at the lower bound of the surface-wave bandgap corresponding to the (c) first longitudinal resonance, (d) first flexural resonance, and (e) second flexural resonance. The mode shape of the resonator-half space unit cell at the upper bound of the surface-wave bandgap corresponding to the (f) first longitudinal resonance, (g) first flexural resonance, and (h) second flexural resonance. The horizontal lines in (b) indicate the resonance (f_R) and anti-resonance (f_A) frequencies of the resonator.

the possible surface wave solutions that propagate on the bottom of the half-space. Finally, eigenfrequency analysis is performed by sweeping the Bloch wavenumber within the irreducible Brillouin zone to obtain the dispersion curves[22]. The commonly employed solid cone method is used to eliminate non-surface wave solutions by limiting the possible wave speeds in the dispersion curves to be less than the transverse wave speed[22]. Three surface-wave bandgaps are observed from the dispersion curves in Fig. 4 (b), one corresponding to the longitudinal resonance (449-532 kHz) and the other two due to the flexural resonances (323-329 kHz and 767-803 kHz) of resonators. It is clear from the dispersion curves that the longitudinal resonance creates a wide bandgap that can be exploited for different applications. On the other hand, band gaps due to flexural resonances are narrow, in agreement with the findings from previous studies[15].

Mode shapes corresponding to the lower bounds of the bandgaps depict the longitudinal

(Fig. 4 (c)) and flexural (Figs. 4 (d) and 4 (e)) vibrations of the resonator. As expected, the frequencies defining these lower bounds closely match the coupled resonance frequencies (marked in Fig. 4(b)) estimated earlier from the analysis of a single resonator (Fig. 3(d)). However, a slight discrepancy between the coupled resonance frequencies determined for a single resonator and an array of resonators is expected, as the coupled resonance frequency is influenced by the number of resonators[17]. All the three mode shapes at the lower bounds exhibit significant displacement in the resonator with near-zero displacement of the half-space, suggesting no possible surface waves propagating at these frequencies. The mode shapes at the upper bounds (Figs. 4(f), 4(g), and 4(h)) are similar to those observed at lower bounds, but show slight deformations of the half-space. Since the mode shapes at the upper bounds are extracted along the transverse wave sound line, the observed deformations of the half-space correspond to the propagating transverse waves. The U_1 and U_3 displacement anti-resonance frequencies of the resonator estimated earlier from the single resonator analysis are marked in Fig. 4(b). The U_3 displacement anti-resonance frequency lies within the longitudinal-resonance bandgap obtained from the dispersion analysis, suggesting the efficiency of an array of Mindlin BC patches (imposed by resonators) in suppressing Rayleigh waves[16]. In contrast, the U_1 displacement anti-resonance frequencies fall outside the flexural-resonance bandgaps, as expected considering the inefficiency of Auld BC patches (imposed by resonators) in suppressing Rayleigh waves[16]. Next, we study how the presence of an array of resonators influences the clamping conditions at the resonance and anti-resonance frequencies.

2. Anti-resonance analysis

Here, we perform a frequency-domain finite element analysis similar to that shown in Fig. 2(a), but with an array of 30 resonators (along the wave propagation) mounted on the "resonator" region (Fig. 5(a)). The spacing between the resonators is consistent with the size of the unit cell used for generating dispersion curves (Fig. 4 (a)). A frequency sweep from 250 kHz to 850 kHz with increments of 5 kHz is employed to perform a parametric frequency-domain study. As an example, the anti-resonance displacement (abs(U_1) and abs(U_3)) profiles at the base of the 20^{th} resonator are shown in Fig. 5 (b). The surface-wave bandgaps obtained from the dispersion analysis are highlighted in grey for comparison.

Similar to the case of a single resonator, the U_3 (510 kHz) and U_1 (335 kHz and 815 kHz) displacement anti-resonance frequencies (marked in Fig. 5(b)) can be observed for an array of resonators, suggesting that the anti-resonance frequencies are not changed by the presence of multiple resonators. Analyzing the U_3 and U_1 displacements at the base of the 1^{st}, 10^{th}, 20^{th}, and 30^{th} resonators, confirms the presence of U_3 and U_1 displacement anti-resonances across the resonator array (Fig. 5(c)). The observed gradually decreasing displacement amplitude for the later resonators (the 10^{th}, 20^{th} and 30^{th}) is expected considering the successive mode conversion of Rayleigh wave to transverse waves by the resonators, which transmits energy away from the surface[16].

To further corroborate the imposing of Mindlin and Auld BCs at the corresponding anti-resonance frequencies, we compare the frequency-domain displacement (real(U_3)) fields for an array of BC patches and an array of resonators at the resonator's anti-resonance frequencies. To that end, we consider a similar COMSOL model as in Fig. 5(a) but with 30 frequency-independent BC patches, each having the size of one resonator base, positioned in the place of resonators. The boundary conditions over these patches are varied as Mindlin, Auld, and Dirichet BCs. The displacement (real(U_3)) fields corresponding to the anti-resonance frequencies (335 kHz, 510 kHz, 815 kHz) observed in Fig. 5 (b) are shown in Figs. 5(e), 5(g), and 5(i). The simulation results for an array of Mindlin BC patches at frequencies 510 kHz ((Fig. 5 (m)), and an array of Auld BCs at frequencies 335 kHz and 815 kHz (Figs. 5 (k) and 5 (o)) are shown in Fig. 5. A close similarity between the displacement fields at 510 kHz for the simulations involving resonators and Mindlin BC patches can be observed (Figs. 5 (g) and 5 (m)). Although the Auld BC patch simulation results match closely the results corresponding to the case with the resonator array at 815 kHz anti-resonance frequency (Figs. 5 (i) and 5 (o)), they do not seem to match at the 335 kHz (Figs. 5 (e) and 5 (k)) anti-resonance frequency. A possible reason is that the resonators do not impose perfect Auld BCs. Some deviations between the two sets of displacement fields are expected as the resonators constrain both the displacement components, whereas over the Mindlin and Auld BC patches, one of the displacement components remains unconstrained.

An interesting observation is that the additional anti-resonances corresponding to the displacements $abs(U_1)$ and $abs(U_3)$ at frequencies (325 kHz, 460 kHz, and 785 kHz - marked in Fig 5(b)) are close to the coupled resonance frequencies (325 kHz, 455kHz, and 775 kHz) obtained earlier for the case of a single resonator (Figs. 2(d)). These additional

Journal of Applied Physics

PLEASE CITE THIS ARTICLE AS DOI: 10.1063/5.0093083

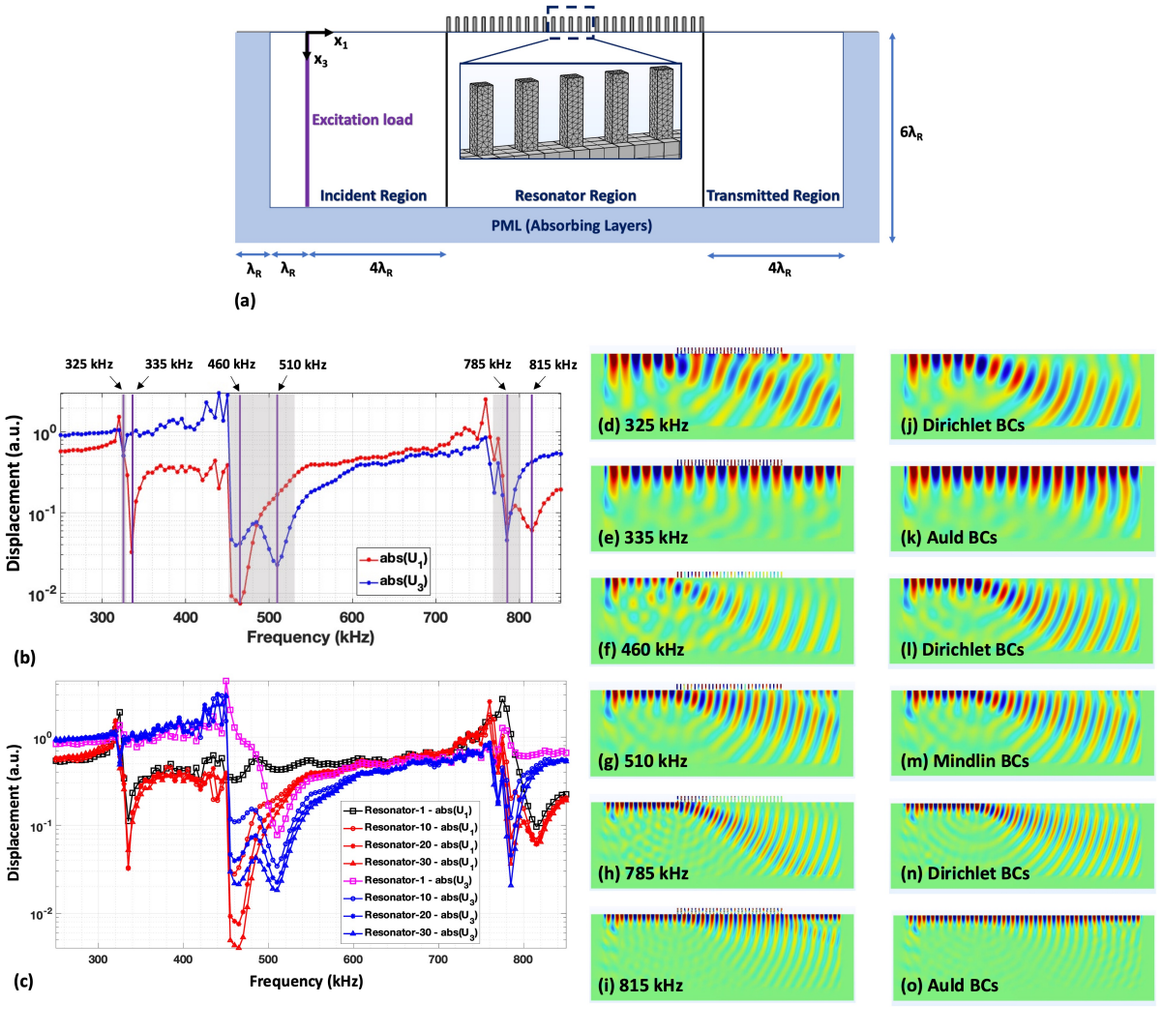

FIG. 5. (a) Schematic of a traction-free elastic half-space with an array of 30 resonators surface-mounted on the "resonator" region. (b) The anti-resonance profiles (abs(U_1) and abs(U_3)) corresponding to the base of the 20^{th} resonator in the path of Rayleigh wave propagation. (c) The anti-resonance profiles (abs(U_1) and abs(U_3)) corresponding to the base of the 1^{st}, 10^{th}, 20^{th}, and 30^{th} resonator in the path of the Rayleigh wave propagation. The frequency-domain simulation results depicting the real(U_3) displacement fields at the resonance ((d) 325 kHz, (f) 460 kHz, and (h) 785 kHz) and anti-resonance ((e) 335 kHz, (g) 510 kHz, and (i) 815 kHz) frequencies. The frequency-domain simulation results depicting the real(U_3) displacement field for an array of 30 BC patches that impose Dirichlet BCs ((j) 325 kHz, (l) 460 kHz, and (n) 785 kHz)), Mindlin BCs ((m) 510 kHz), and Auld BCs ((k) 335 kHz and (o) 815 kHz) in the direction of Rayleigh wave propagation.

anti-resonance frequencies match closely the frequencies at which maximum transmission dips are observed (325 kHz, 455 kHz, and 780 kHz) in the transmission spectrum (as will be demonstrated later) within the longitudinal and flexural bandgaps. Therefore, these frequencies potentially represent the coupled resonance frequencies considering the influence of a resonator array[17]. Both displacement components, $abs(U_1)$ and $abs(U_3)$, are very small around 460 kHz and 785 kHz, which may be interpreted as imposing Dirichlet BCs ($U_1 = 0$, $U_3 = 0$) in the path of Rayleigh wave propagation. In line with these observations, we observe that the displacement fields ($real(U_3)$) for an array of resonators (Figs. 5(f) and 5(h)) at these resonance frequencies (460 kHz and 785 kHz) correlate well with that of an array of Dirichlet BC patches (Figs. 5(l) and 5(n)). Similarly, there is also a slight drop in the U_3 displacement before the U_1 displacement anti-resonance at 335 kHz (Figs. 5(b)). However, the decrease is not significant compared to that observed at 460 kHz or 785 kHz, and U_1 displacement anti-resonance does not seem to exist at 325 kHz, unlike what is observed at 785 kHz. This inconsistency can also be witnessed by comparing the frequency-domain displacement fields (real(U_3)) for an array of resonators (Fig. 5(d)) with that of Dirichlet BC patches (Fig. 5(j)). Although the displacement fields for the resonators at 325 kHz and Dirichlet BC patches are similar in terms of the mode-converted transverse waves, we see the presence of slow-moving Rayleigh waves in the case of the resonator array (Fig. 5(d)). This indicates that imposing Dirichlet BCs at frequencies within the surface-wave bandgap - generated by the first flexural resonance of the resonator with the U_1 and U_3 displacement anti-resonance in Fig. 5(b) - is obscured because of the narrow flexural resonance bandgap. Preforming a frequency sweep with a finer resolution would possibly provide a better visualization of imposing Dirichlet BCs at 325 kHz.

Moreover, Fig. 5(c) illustrates that the U_3 and U_1 anti-resonance displacement profiles of the first resonator in the array match closely those of a single resonator (Fig. 2(b)) due to the absence of Rayleigh wave dispersion and indicate no dips at the resonance frequencies (325 kHz, 460 kHz, and 785 kHz). However, the dips are evident for the rest of the resonators shown in Fig. 5(c). Fig. 6 shows the displacement (abs(U_1) and abs(U_3)) fields close to the resonator array at the resonance frequencies (460 kHz and 785 kHz). At 460 kHz, we observe the clamping conditions at the base of resonators in the array, excluding the first couple, to resemble Dirichlet BCs ((abs(U_1) $\sim$ 0, abs(U_3) $\sim$ 0)), with resonators exhibiting longitudinal mode shapes (Figs. 6 (a) and 6(b)). On the other hand, at the 785 kHz excitation frequency,

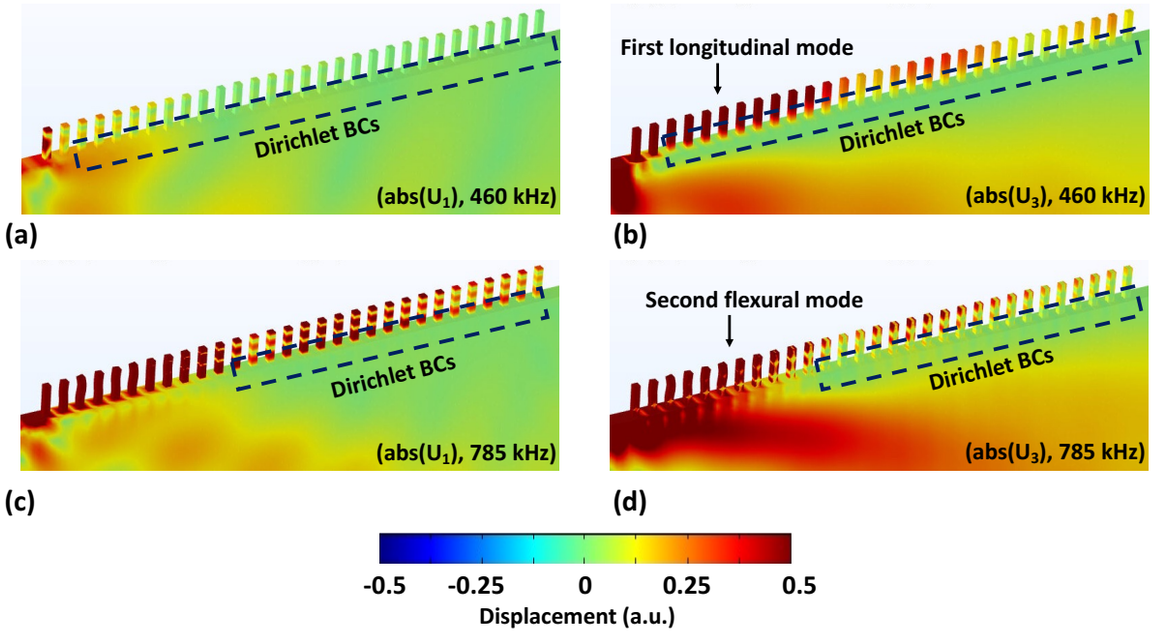

FIG. 6. The frequency-domain simulation results depicting the displacement fields closer to the surface-mounted resonators at frequencies 460kHz ((a) abs(U_1) and (b) abs(U_3)) and 785 kHz ((c) abs(U_1) and (d) abs(U_3)).

Dirichlet BCs seem to be imposed at the base of the resonators after the 10^{th} resonator, with resonators exhibiting flexural mode shapes (Figs. 6(c) and 6(d)).

Next, we study the transmission characteristics demonstrated by the resonator array in relation to the above analysis of the clamping conditions imposed by the resonators at the resonance and anti-resonance frequencies. Such a study is necessary to comment on the efficiency of the meta-surface to suppress Rayleigh waves at the U_3 displacement anti-resonance frequency.

3. Transmission characteristics

For each excitation frequency, the transmission spectrum (Fig. 7(a)) is obtained by performing SFT over the complex displacement data ($U_1 + U_3$) extracted along the top surfaces of the "incident" and "transmitted" regions. The surface-wave bandgaps obtained earlier through the dispersion analysis, and the resonance and anti-resonance frequencies obtained from the analysis of a single resonator are highlighted in the transmission spectrum

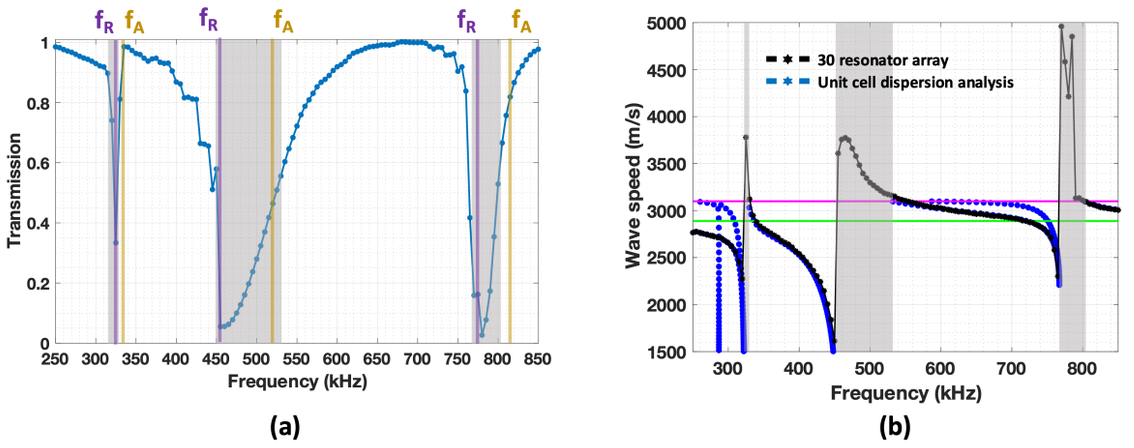

FIG. 7. (a) The transmission spectrum obtained for an array of 30 resonators surface-mounted on the "resonator" region. (b) The wave speed-frequency dispersion curves, obtained by applying the spatial Fourier transform on the complex displacement data extracted on the top surface of the "resonator" region in comparison to that obtained from the unit cell dispersion analysis. The highlighted grey regions in (a) and (b) indicate the surface-wave bandgaps found through the unit cell dispersion analysis. The vertical lines in (a) indicate the resonance (f_R) and anti-resonance (f_A) frequencies of the resonator. The horizontal lines in (b), colored in magenta and green, indicate the transverse and Rayleigh wave speeds, respectively.

(Fig. 7(a)) for comparison. It is evident that the drops in the transmission spectrum coincide with the expected longitudinal and flexural resonance bandgaps, suggesting that the dispersion induced by local resonances is included in the numerical model with 30 resonators. Coherent with our understanding of how the Rayleigh wave interacts with Mindlin BCs[16], it appears that both resonance and anti-resonance of the resonators are responsible for the longitudinal-resonance bandgap (Fig. 7(a)). However, only the resonance is responsible for the flexural-resonance bandgap because the U_1 displacement ant-resonance (Auld BCs) cannot suppress Rayleigh wave propagation[16].

By performing a similar SFT analysis over the complex displacement data ($U_1 + U_3$) extracted along the top surface of the "resonator" region, it is also possible to generate the Rayleigh wave dispersion curves for the metasurface. The wave speed-frequency dependency obtained from the SFT analysis for different excitation frequencies is plotted against the dispersion curves extracted from the unit cell, as shown in Fig. 7(b). As expected from a local-

resonance phenomenon, the phase speed approaches a minimum (theoretically, it should approach zero) at the coupled resonance frequencies (at the lower bounds of the bandgaps) (Fig. 7(b)). Inside the bandgap, we see a sudden increase in wave speed with values reaching above the transverse wave speed due to the mode-converted transverse waves propagating at an oblique angle. It is important to note that the SFT applied over the horizontally spaced data points (along the x_1 direction), gives information on the wavenumber components in the x_1 direction. Therefore, the apparent wave speed values will appear larger than the real speed of transverse waves traveling into the half-space at an angle. On a related note, the variation of wave speed within the bandgap, estimated using the x_1 wavenumber component, is linked to the variation in the propagation angles of the mode-converted transverse waves (Fig. 7(b)).

For example, we can observe the change in wave propagation angles of the mode-converted waves within the longitudinal-resonance bandgap with change in clamping conditions from Dirichlet BCs imposed at the resonance frequencies to Mindlin BCs imposed at the anti-resonance frequencies (see Figs. 5 (f) and 5 (g)). As expected from the BC patch study (See supplementary material), imposing the Dirichlet BCs will result in transferring more energy from incident Rayleigh wave at broader angles deeper into the half-space. In comparison, the Mindlin BCs result in mode-converted transverse waves that propagate closer to the surface[16]. The larger the mode-converted wave propagation angles, the greater will be the transmission loss. In other words, this analysis suggests that the hybridization between the incident Rayleigh wave and the coupled longitudinal resonance of the resonator offers significant Rayleigh wave suppression compared to that obtained at the anti-resonance frequency of the resonator where Mindlin BCs are imposed, providing a new perspective on the asymmetry observed in the transmission drop profile. In contrast, since only the resonance frequencies play a role in generating the flexural resonance bandgap, the transmission bandgap appears more symmetric.

In comparison to the 8% Rayleigh wave suppression achieved for a single resonator (Fig. 2(c)) in the direction of wave propagation, an array of 30 resonators demonstrated 63% suppression at the U_3 displacement anti-resonance frequency (Fig. 7(a)). This indicates that though an array of Mindlin BC patches are effective in comparison to a single Mindlin BC patch, the Rayleigh wave suppression could still be less because many factors such as resonator width, resonator spacing, and a number of resonators are expected to play a

role on the transmission characteristics for an array of Mindlin BC patches. The reported frequency-independent BC patch investigations and frequency-dependent resonator studies provide an in-depth understanding of the role of resonances and anti-resonances in shaping the longitudinal and flexural resonance bandgaps. In the next session, we discuss the possible widening of the longitudinal resonance bandgap by manipulating the resonances and anti-resonances to motivate anti-resonance-matched resonator design strategies using topology optimization.

III. DISCUSSION

The coupled resonance frequencies depends on many factors, such as the resonator mass, equivalent stiffness of the resonator and substrate, and the number of resonators[17]. Given the complexity of the analytical framework to determine the coupled resonance frequencies for rod-like resonators[17] and solution to the boundary value problem of the rod resonators mounted on the half-space[15], we resort to employing numerical finite element software to evaluate these frequencies. As previously demonstrated, evaluating the onset of the bandgap using the eigenfrequency analysis of a unit cell or the frequency corresponding to the resonator's maximum relative displacement response can help determine the resonance frequencies. On the other hand, estimating the anti-resonance frequency of the rod-like resonator in the path of Rayleigh wave propagation is straightforward as it is equivalent to the eigenfrequency of the resonator subject to fixed-free or Mindlin-free BCs.

It is important to note that resonance and anti-resonance corresponding to longitudinal vibrations govern the extent of the longitudinal resonance bandgap, and it is possible to broaden the bandgap by pushing the resonance frequency away from the anti-resonance frequency. Earlier studies demonstrated the possible widening of the bandgap by varying the filling fraction, resonator spacing, number of resonators etc.[17,22] However, an understanding of the influence of these parameters on the resonance and anti-resonance frequencies and their integrated effect on the widening/narrowing of the bandgap is lacking. Here, we present a parametric case study of an array of 30 resonators by varying the filling fraction and resonator spacing to understand the influence of resonance and anti-resonance frequencies in shaping the bandgaps (Fig. 8). In the first case, we keep the resonator spacing/lattice length (A = 1 mm, 1.5 mm, and 2 mm) constant varying the filling fraction (W^2/A^2) from

0 to 0.5, whereas in the second case, we keep the resonator width constant (W = 0.5 mm, 0.75 mm, and 1 mm) and vary the lattice length (A) from 0.8 mm to 2 mm. In both cases, a 2.5 mm resonator length is chosen to obtain the anti-resonance frequency around 500 kHz ($\sim$ 510 kHz). We consider all the possible cases with a resonator width and a unit cell filling fraction less than 1 mm and 0.5, respectively. An upper limit on the resonator width is imposed to maintain an aspect ratio (L/W) of at least 2.5 for the resonator, whereas an upper limit on the filling fraction is considered because the flexural resonances at higher filling fractions are observed to interfere with the longitudinal-resonance bandgaps.

A. Filling fraction

Increasing the filling fraction for a constant lattice length is observed to decrease the resonance frequency (Fig. 8(b)), as expected due to the increase in resonator mass[17]. Moreover, resonance frequency decreases with an increase in the lattice length for a constant filling fraction (Fig. 8(b)). Although the anti-resonance frequency does not change with the filling fraction or lattice length, the transmission characteristics at the anti-resonance frequencies vary. Fig. 8(c) demonstrates a decrease in Rayleigh wave transmission for an array of resonators at the anti-resonance frequency (510 kHz) with an increase in filling fraction. For comparison, we also demonstrate the Rayleigh wave transmission for a similar array of frequency-independent Mindlin BC patches, with each patch of the same size as the resonator base. Fig. 8(d) shows a similar trend in comparison to Fig. 8(c) but with a small difference in the Rayleigh wave transmission. This is expected because of slightly imperfect imposing of Mindlin BCs by resonators at the resonator's anti-resonance frequency compared to perfect Mindlin BC patches. For a given filling fraction, the Rayleigh wave transmission increases with the lattice length for a smaller filling fraction but decreases for a higher filling fraction (Figs. 8(c) and 8(d)). This is because of two competing mechanisms exhibited by an array of Mindlin BC patches that influence the transmission characteristics at the anti-resonance frequency: (1) increasing the Mindlin BC patch width for a constant patch spacing decreases the Rayleigh wave transmission and (2) increasing the Mindlin BC patch spacing for a constant patch length increases the Rayleigh wave transmission. Therefore, for a smaller filling fraction, the influence of patch spacing dominates the transmission spectrum, whereas the patch width dominates the transmission spectrum for a higher filling

Journal of Applied Physics

AIP Publishing

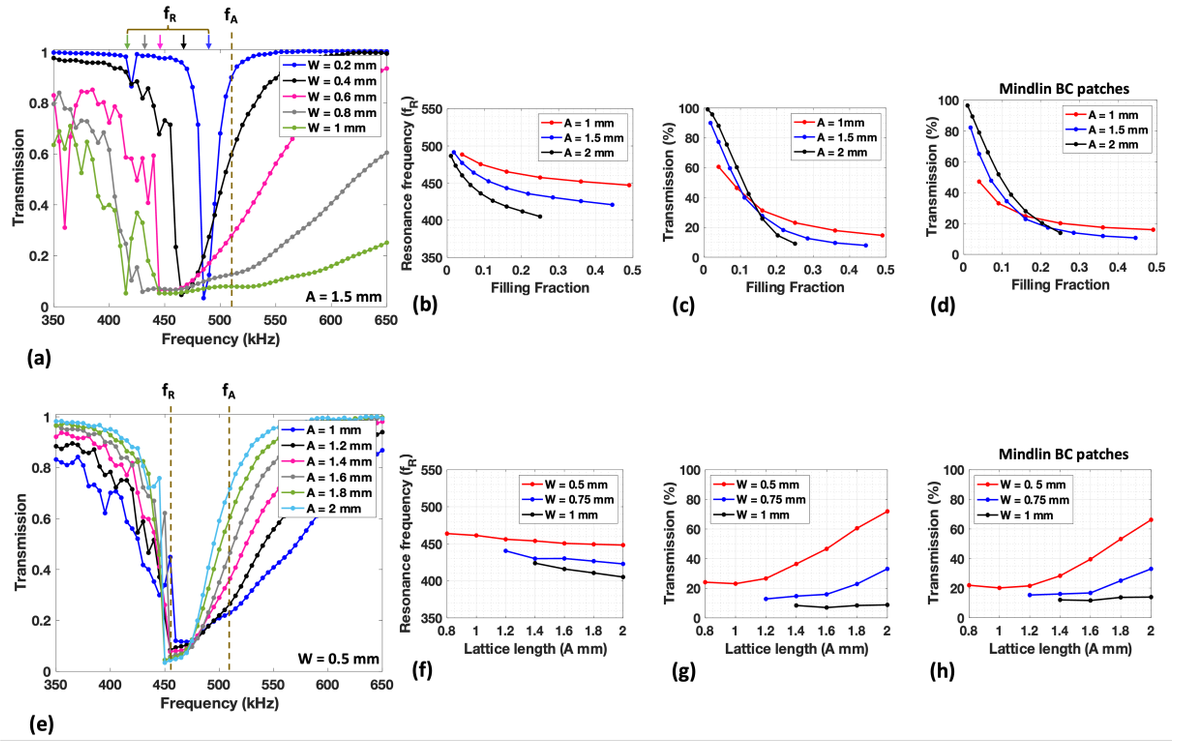

FIG. 8. Parametric analysis on an array of 30 resonators to study the influence of filling fraction and lattice length on the resonance frequencies and the transmission characteristics at the anti-resonance frequencies. (a) The transmission spectra obtained for a constant lattice length of 1.5 mm and a range of resonator widths (W = 0.2 mm to 1 mm). Variation of (b) resonance frequencies and the Rayleigh wave transmission for an (c) array of resonators and an (d) array of Mindlin BC patches with the filling fraction keeping the lattice length constant (A = 1 mm, 1.5 mm and 2 mm). (e) The transmission spectra obtained for a constant resonator width of 0.5 mm and a range of lattice lengths (A = 1 mm to 2 mm). Variation of (f) resonance frequencies and the Rayleigh wave transmission for an (g) array of resonators and an (h) array of Mindlin BC patches with the lattice length keeping the resonator width constant (A = 0.5 mm, 0.75 mm and 1 mm).

fraction. To summarize, increasing the filling fraction for a constant lattice length/resonator spacing decreases the coupled resonance frequency and the Rayleigh wave transmission at the anti-resonance frequency and widens the longitudinal resonance surface-wave bandgap by expanding both the lower and upper bounds. As an example, the transmission spectrum for different resonator widths (0.2 mm to 1 mm) at a constant lattice length (1.5 mm) is shown in Fig. 8(a), demonstrating the widening of bandgap in both the directions.

B. Lattice length

In contrast to the effect of filling fraction, increasing the lattice length for a given resonator width seems to have a minimal influence on the coupled resonance frequency, as shown in Fig 8(f). As expected from earlier observations, the Rayleigh wave transmission increases with the lattice length, both for the cases of resonators at the anti-resonance frequency (Fig. 8(g)) and perfect Mindlin BC patches (Fig. 8(h)). However, the increase in transmission is significantly smaller at higher lattice lengths for larger resonator widths (Figs. 8(g) and 8(h)). To summarize, increasing the lattice length for a given resonator diameter has a minimal influence on the resonance frequency but increases the Rayleigh wave transmission at the anti-resonance frequency. This results in narrowing the longitudinal bandgap at the upper bound with minimal frequency shift observed at the lower bound, as demonstrated in the transmission spectra (Fig 8(e)) for different lattice lengths (1 mm to 2 mm) while maintaining the resonator width constant (0.5 mm). On the other hand, an increase in the number of resonators is expected to decrease the Rayleigh wave transmission at the anti-resonance frequency as each of the Mindlin BC patches converts a portion of the Rayleigh wave to a transverse wave. Therefore an increase in the number of resonators is expected to broaden the longitudinal resonance bandgap towards the upper bound until zero transmission at the anti-resonance frequency is achieved.

These observations indicate possible enhanced suppression of Rayleigh waves at the anti-resonance frequencies, motivating a systematic design of optimized resonators based on matching the anti-resonance frequency corresponding to the U_3 displacement with the incident Rayleigh wave frequency through topology optimization. Moreover, exploiting the design parameters that maximize the separation between the resonance and anti-resonance frequencies, for example by increasing the mass of the resonator, wide bandgaps can be realized. One of the main benefits of such an approach is that it enables designing resonators without the need to couple the resonator to the half-space. Therefore, a rational design procedure for resonators is possible beyond the state-of-the-art approach, which requires an extensive parametric eigenfrequency analysis over a unit cell comprising a resonator and half-space[18–21].

IV. CONCLUSION

Drawing insights from the interaction of Rayleigh waves with different frequency-independent BCs (Mindlin, Auld and Dirichlet BCs)[16], we study how the resonances and anti-resonances of prismatic surface-mounted resonators in the path of a Rayleigh wave shape the longitudinal and flexural-resonance surface-wave bandgaps. Two cases are presented: a single resonator and an array of closely spaced resonators. A single resonator demonstrates poor Rayleigh wave suppression at both its vertical (U_3) and horizontal (U_1) displacement anti-resonance frequencies; the former is because of the inefficiency of Auld BCs to suppress Rayleigh waves, and the latter is due to the small resonator width, hence the small-sized imposed Mindlin BC patch . Despite its poor transmission characteristics, through an analysis of a single resonator, we demonstrate that a vertical harmonic traction loading to the resonator base emulates a similar U_3 displacement anti-resonance behavior to that of a resonator mounted in the path of Rayleigh wave propagation. These findings suggest a possible rational design methodology using topology optimization based on matching the U_3 displacement anti-resonance frequencies under vertical forced excitation, the details of which will be reported in a future publication.

For a resonator array, in addition to the longitudinal resonances of the resonators, the U_3 displacement anti-resonances also play a role in the longitudinal resonance surface-wave bandgap formation because an array of Mindlin BCs patches can significantly suppress surface wave motion. However, only the flexural resonances of the resonator appear to be responsible for flexural bandgap formation since flexural anti-resonances resulting in an array of Auld BCs patches do not help suppress Rayleigh waves. Moreover, we demonstrate clamping of both the horizontal and vertical displacement components (Dirichlet BCs) at the longitudinal and flexural resonances of the resonators arranged in a closely-spaced array after the first few resonators, possibly a result of local-resonance induced hybridization. With reference to the clamping conditions realized at the resonances and anti-resonance, we demonstrate poor Rayleigh wave suppression capability at the resonator's anti-resonance frequencies in comparison to that at resonance frequencies. Finally, we demonstrate how the surface-wave bandgaps are shaped in relation to the resonator's resonances and anti-resonances as a result of varying a few key geometric parameters of the unit cell, focusing more on the transmission characteristics of an array of resonators at their anti-resonance

frequencies. Our results demonstrate that the U_3 displacement anti-resonances of closely-spaced resonators having larger base dimensions, can significantly suppress Rayleigh waves. These findings motivate the resonator designs based on matching anti-resonances for applications ranging from seismic isolation of structures to acoustic wave devices.

SUPPLEMENTARY MATERIAL

See supplementary material for the time-domain finite element analysis of the Rayleigh wave interaction with different BCs.

ACKNOWLEDGMENTS

The authors gratefully acknowledge the support of the National Science Foundation under Grant No. 1934527. Any opinions, findings, and conclusions or recommendations expressed in this material are those of the author(s) and do not necessarily reflect the views of the National Science Foundation.

Computations for this research were performed on the Pennsylvania State University's Institute for Computational and Data Sciences' Roar supercomputer.

The authors also thank the reviewers of this manuscript for providing valuable insights which helped improve the quality of the manuscript.

DATA AVAILABILITY STATEMENT

The data that support the findings of this study are available from the corresponding author upon reasonable request.

REFERENCES

[1]P. A. Deymier, *Acoustic metamaterials and phononic crystals*, Vol. 173 (Springer Science & Business Media, 2013).

[2]N. Fang, D. Xi, J. Xu, M. Ambati, W. Srituravanich, C. Sun, and X. Zhang, "Ultrasonic metamaterials with negative modulus," Nature materials **5**, 452–456 (2006).

[3]Z. Liu, X. Zhang, Y. Mao, Y. Zhu, Z. Yang, C. T. Chan, and P. Sheng, "Locally resonant sonic materials," science **289**, 1734–1736 (2000).

[4]A. Palermo, S. Krödel, A. Marzani, and C. Daraio, "Engineered metabarrier as shield from seismic surface waves," Scientific reports **6**, 1–10 (2016).

[5]A. Palermo, S. Krödel, K. H. Matlack, R. Zaccherini, V. K. Dertimanis, E. N. Chatzi, A. Marzani, and C. Daraio, "Hybridization of guided surface acoustic modes in unconsolidated granular media by a resonant metasurface," Physical Review Applied **9**, 054026 (2018).

[6]A. Khelif, Y. Achaoui, S. Benchabane, V. Laude, and B. Aoubiza, "Locally resonant surface acoustic wave band gaps in a two-dimensional phononic crystal of pillars on a surface," Physical Review B **81**, 214303 (2010).

[7]Y. Achaoui, A. Khelif, S. Benchabane, L. Robert, and V. Laude, "Experimental observation of locally-resonant and bragg band gaps for surface guided waves in a phononic crystal of pillars," Physical Review B **83**, 104201 (2011).

[8]A. Colombi, V. Ageeva, R. J. Smith, A. Clare, R. Patel, M. Clark, D. Colquitt, P. Roux, S. Guenneau, and R. V. Craster, "Enhanced sensing and conversion of ultrasonic rayleigh waves by elastic metasurfaces," Scientific Reports **7**, 1–9 (2017).

[9]A. Colombi, P. Roux, S. Guenneau, P. Gueguen, and R. V. Craster, "Forests as a natural seismic metamaterial: Rayleigh wave bandgaps induced by local resonances," Scientific reports **6**, 1–7 (2016).

[10]A. Colombi, D. Colquitt, P. Roux, S. Guenneau, and R. V. Craster, "A seismic metamaterial: The resonant metawedge," Scientific reports **6**, 1–6 (2016).

[11]C. Hakoda, C. J. Lissenden, and P. Shokouhi, "Clamping resonators for low-frequency s0 lamb wave reflection," Applied Sciences **9**, 257 (2019).

[12]C. J. Lissenden, C. N. Hakoda, and P. Shokouhi, "Control of low-frequency lamb wave propagation in plates by boundary condition manipulation," Journal of Applied Physics **129**, 094903 (2021).

[13]E. G. Williams, P. Roux, M. Rupin, and W. Kuperman, "Theory of multiresonant metamaterials for a 0 lamb waves," Physical Review B **91**, 104307 (2015).

[14]M. Rupin, F. Lemoult, G. Lerosey, and P. Roux, "Experimental demonstration of ordered and disordered multiresonant metamaterials for lamb waves," Physical review letters **112**, 234301 (2014).

[15]D. Colquitt, A. Colombi, R. Craster, P. Roux, and S. Guenneau, "Seismic metasurfaces: Sub-wavelength resonators and rayleigh wave interaction," Journal of the Mechanics and Physics of Solids **99**, 379–393 (2017).

[16]L. S. S. Pillarisetti, C. J. Lissenden, and P. Shokouhi, "Control of rayleigh wave propagation through imposing mindlin boundary conditions on the surface," Journal of Sound and Vibration (Accepted) (2022).

[17]X. Pu, A. Palermo, and A. Marzani, "Lamb's problem for a half-space coupled to a generic distribution of oscillators at the surface," International Journal of Engineering Science **168**, 103547 (2021).

[18]Y. Zeng, Y. Xu, K. Deng, Z. Zeng, H. Yang, M. Muzamil, and Q. Du, "Low-frequency broadband seismic metamaterial using i-shaped pillars in a half-space," Journal of Applied Physics **123**, 214901 (2018).

[19]Y. Zeng, S.-Y. Zhang, H.-T. Zhou, Y.-F. Wang, L. Cao, Y. Zhu, Q.-J. Du, B. Assouar, and Y.-S. Wang, "Broadband inverted t-shaped seismic metamaterial," Materials & Design **208**, 109906 (2021).

[20]Y. Zeng, Y. Xu, H. Yang, M. Muzamil, R. Xu, K. Deng, P. Peng, and Q. Du, "A matryoshka-like seismic metamaterial with wide band-gap characteristics," International Journal of Solids and Structures **185**, 334–341 (2020).

[21]Q. Du, Y. Zeng, Y. Xu, H. Yang, and Z. Zeng, "H-fractal seismic metamaterial with broadband low-frequency bandgaps," Journal of Physics D: Applied Physics **51**, 105104 (2018).

[22]Y.-f. Liu, J.-k. Huang, Y.-g. Li, and Z.-f. Shi, "Trees as large-scale natural metamaterials for low-frequency vibration reduction," Construction and Building Materials **199**, 737–745 (2019).

[23]"COMSOL Multiphysics, User's Manual Version 5.6, COMSOL Inc, 2020," .

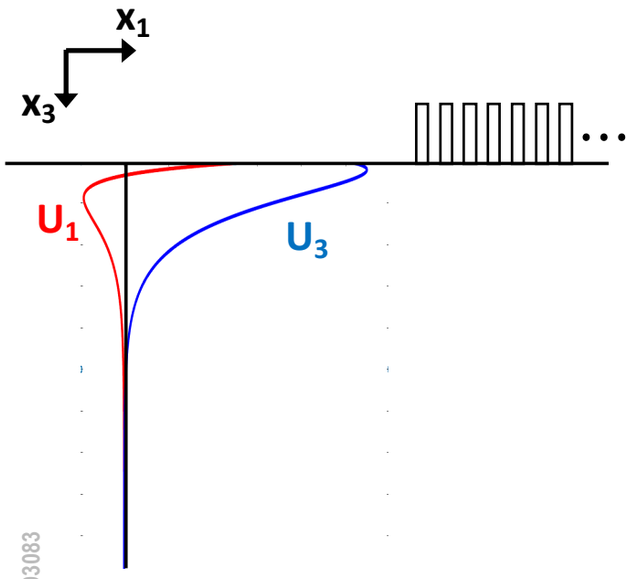

(a)

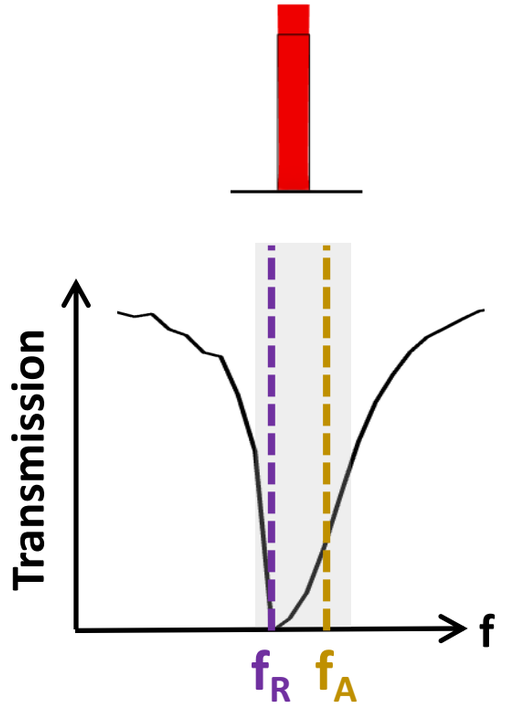

Longitudinal-resonance bandgap

(b)

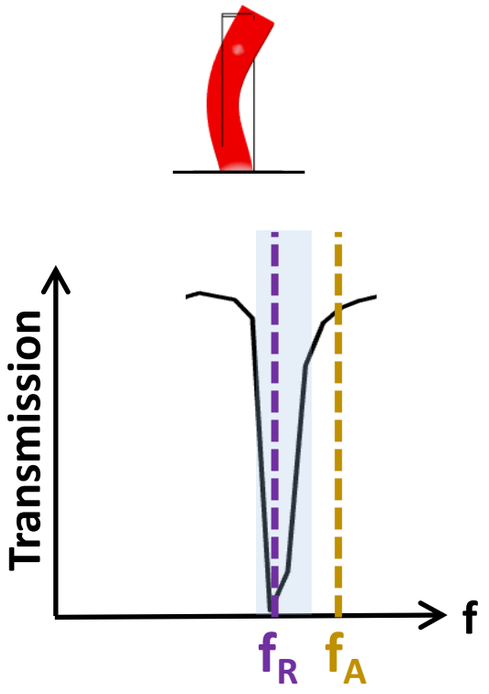

Flexural-resonance bandgap

(c)

Journal of Applied Physics

AIP Publishing

DOI: 10.1063/5.0093083

Journal of Applied Physics

AIP Publishing

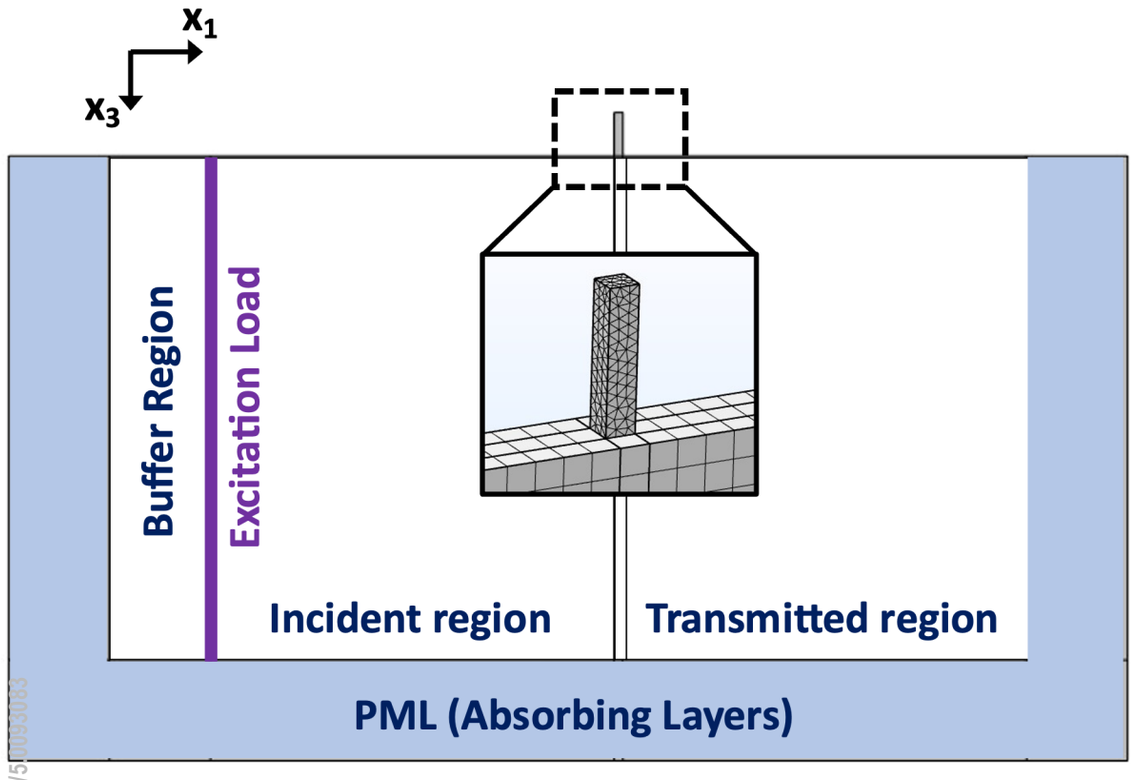

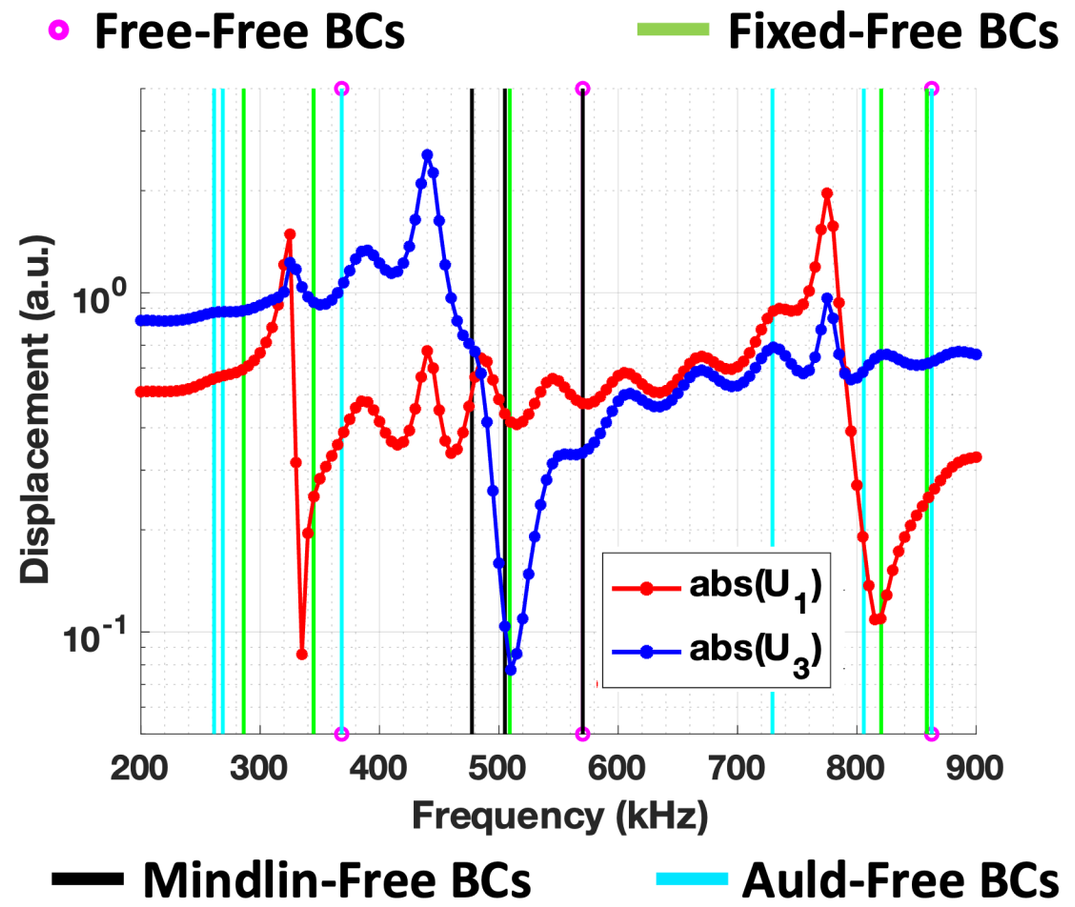

(a)

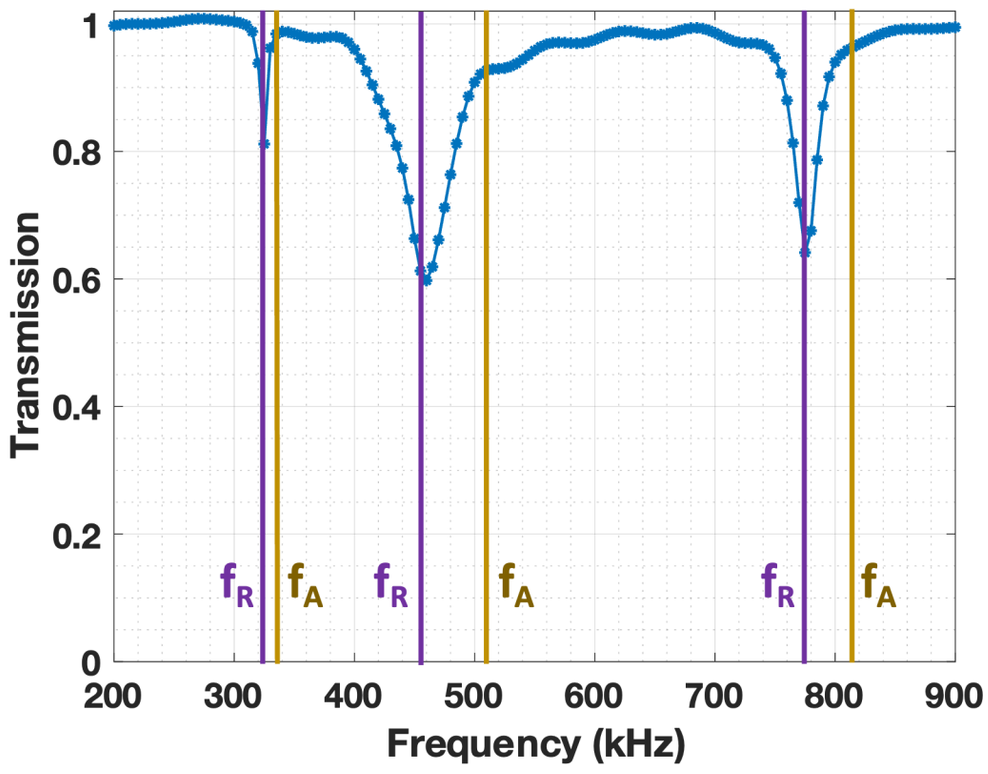

(b)

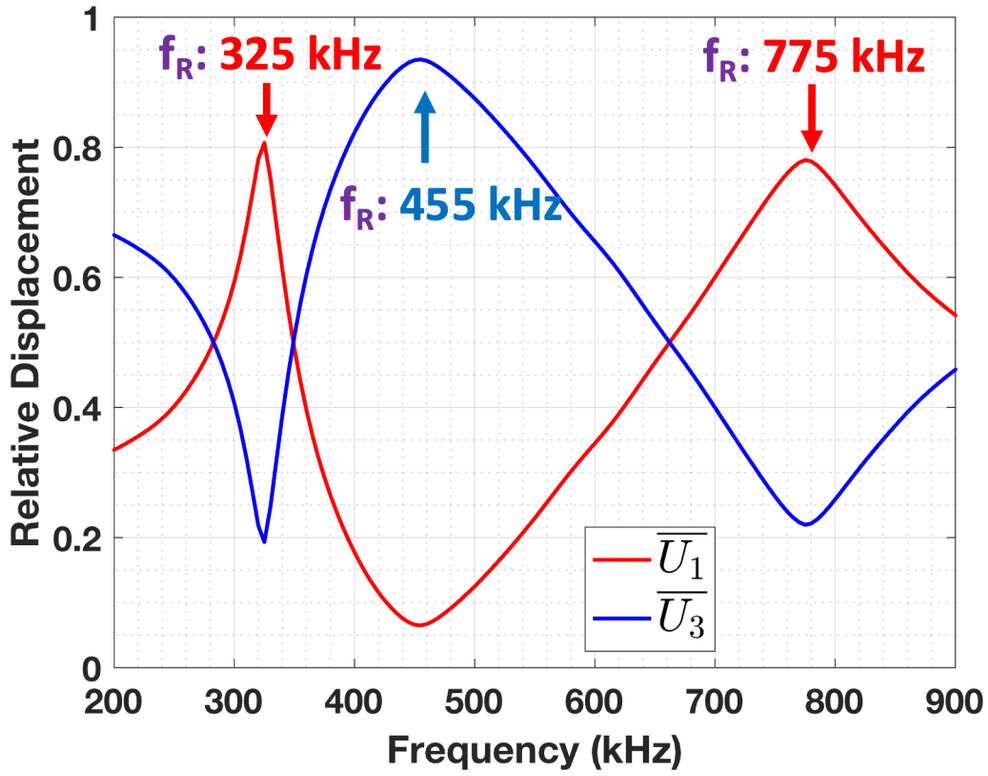

(c)

(d)

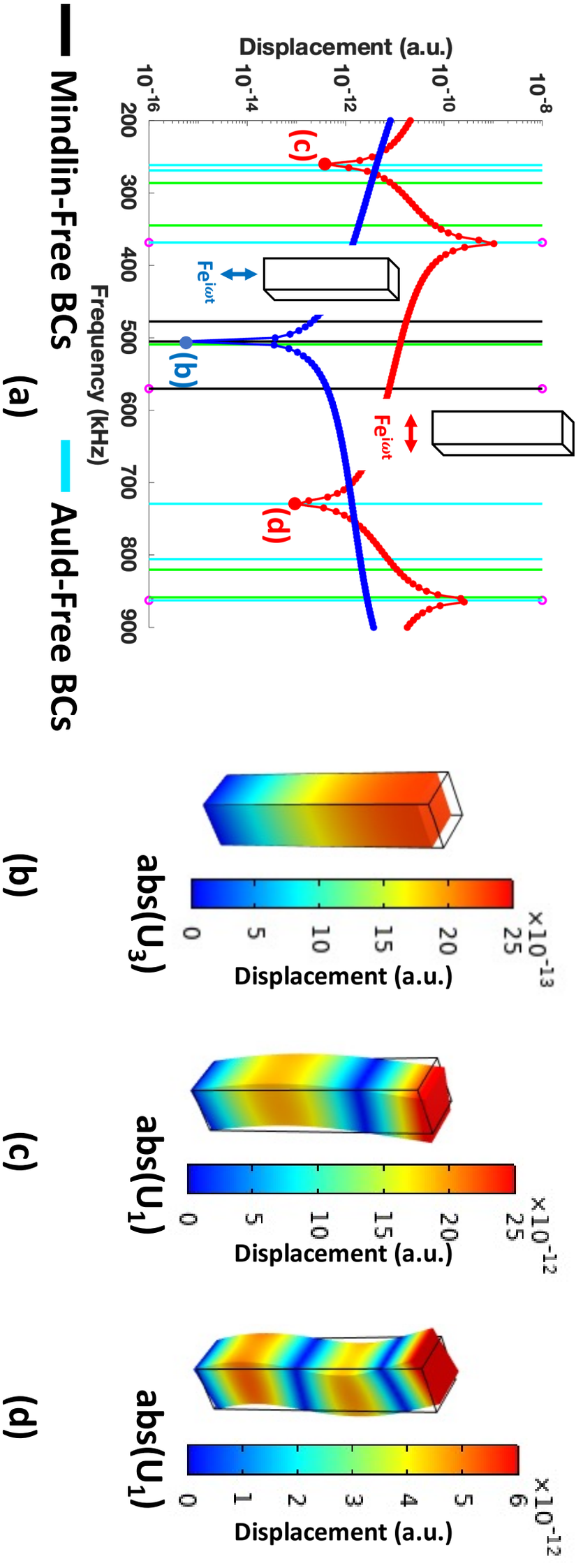

PLEASE CITE THIS ARTICLE AS DOI: 10.1063/5.0093083

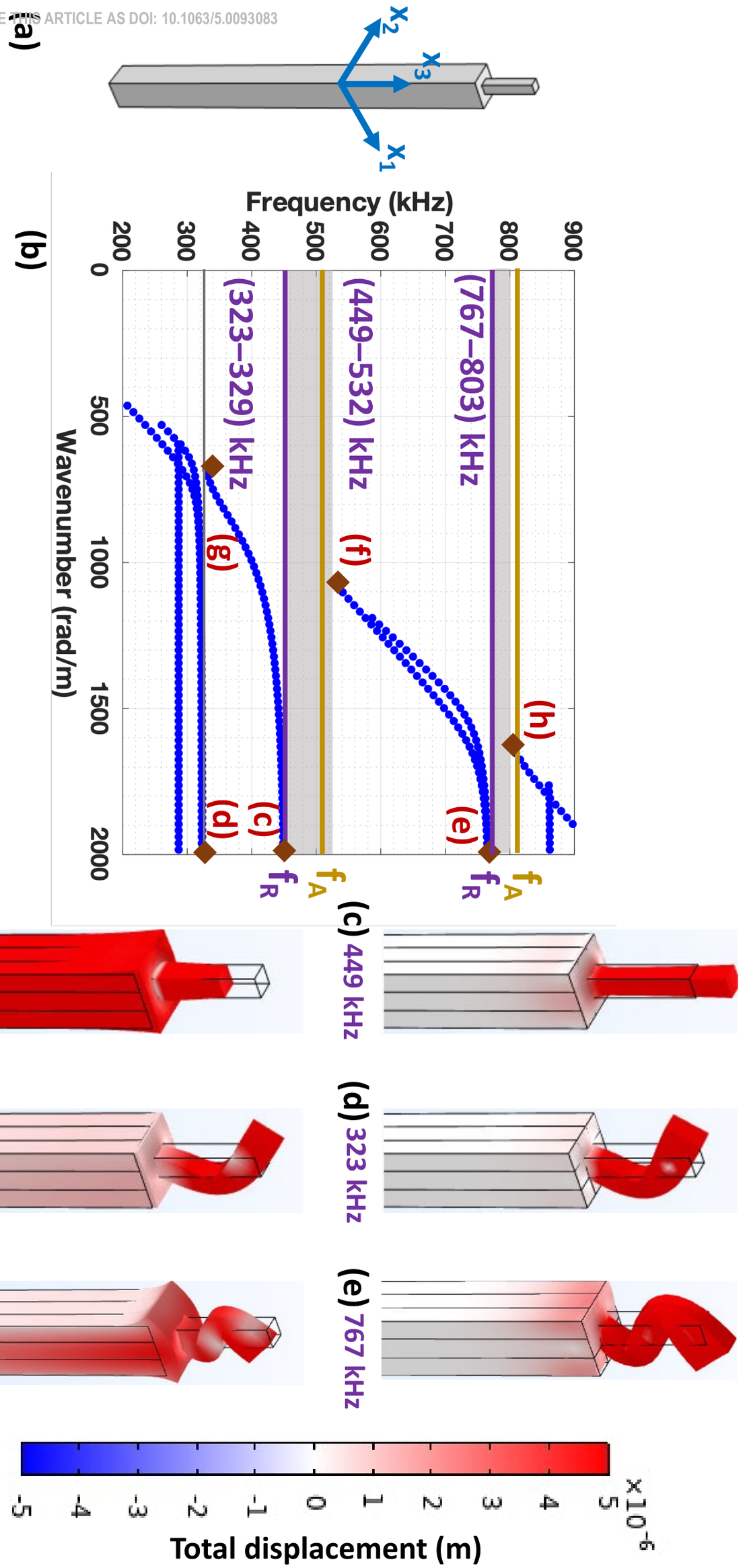

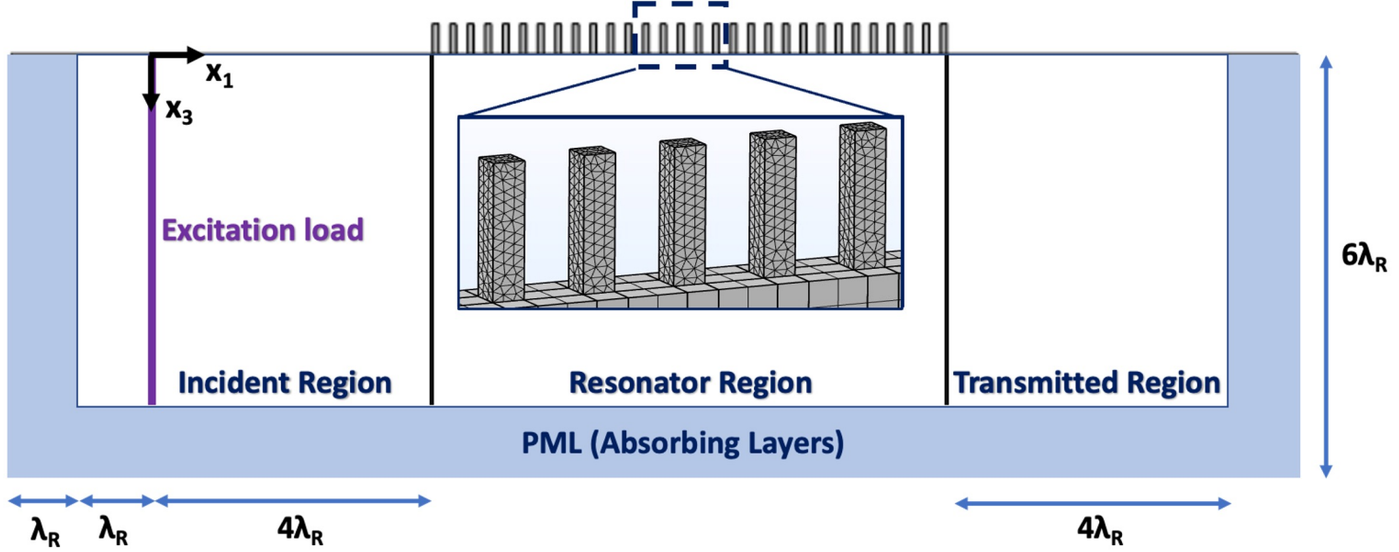

(a)

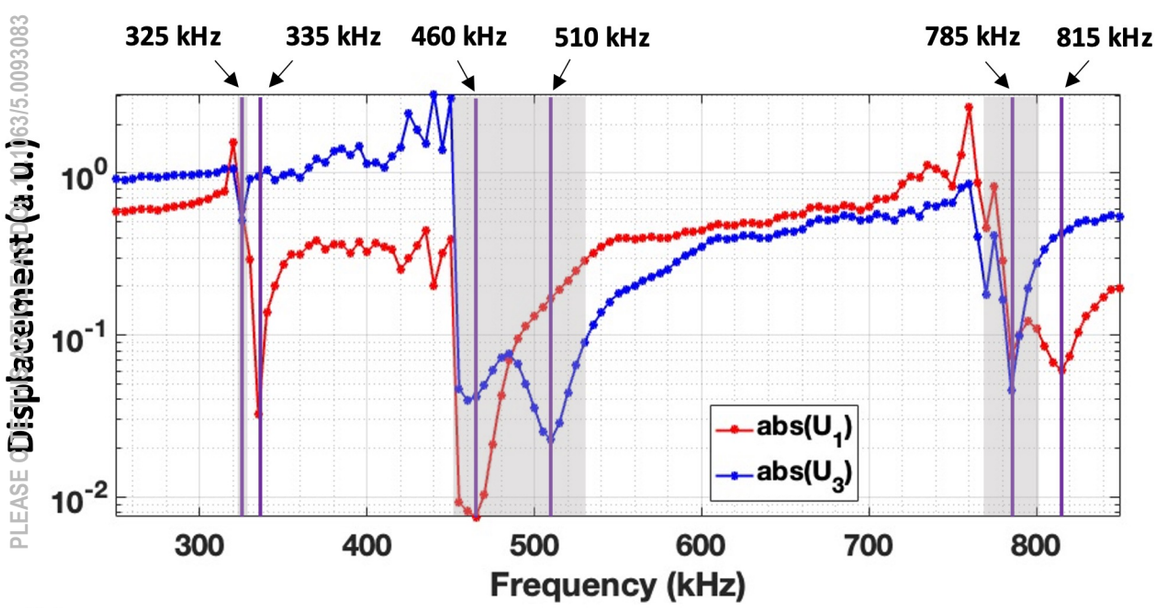

(b)

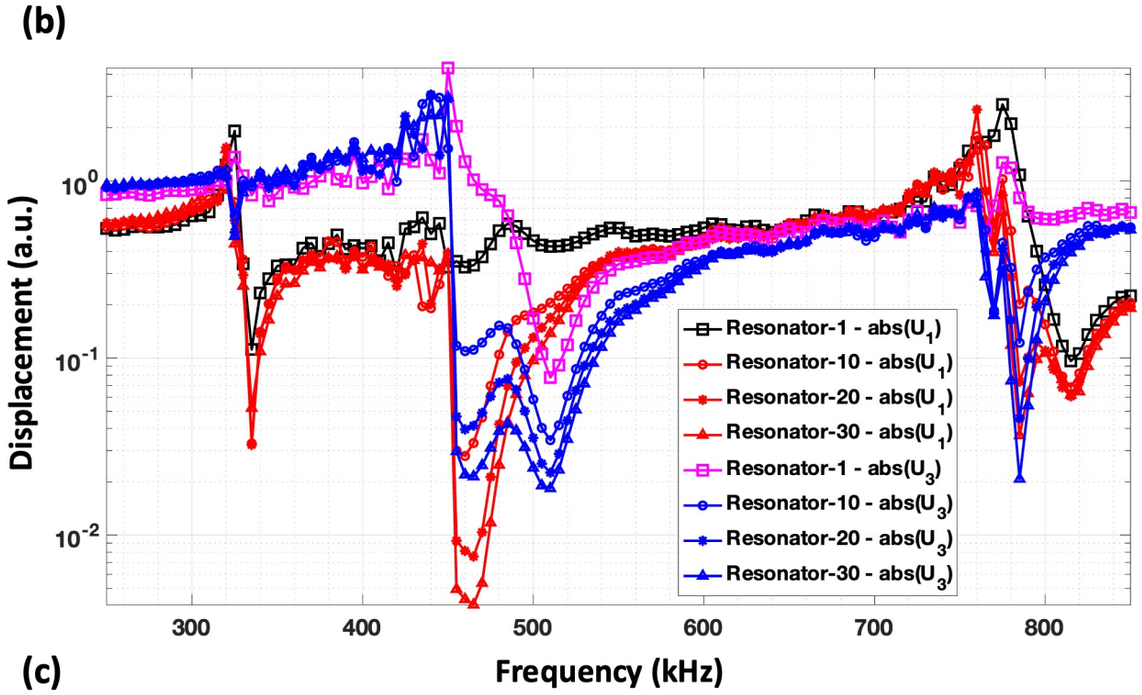

(c)

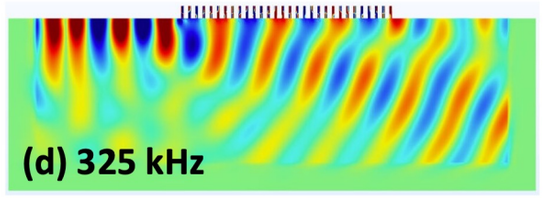
(d) 325 kHz

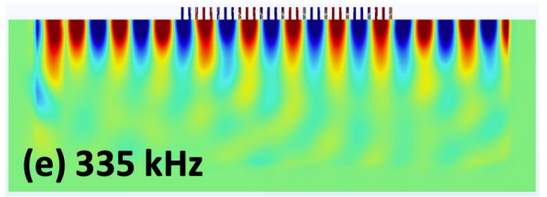
(e) 335 kHz

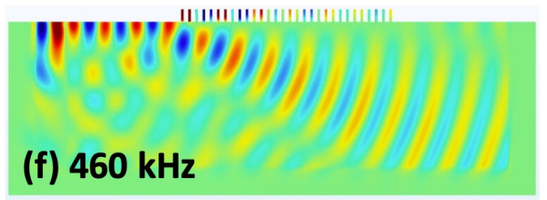
(f) 460 kHz

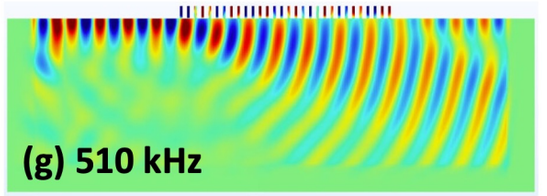
(g) 510 kHz

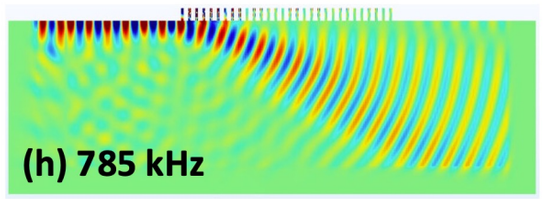
(h) 785 kHz

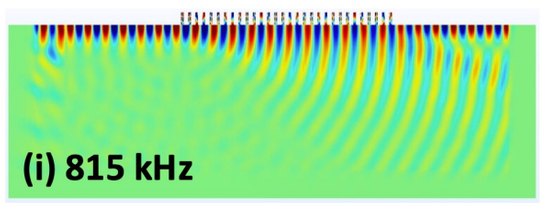
(i) 815 kHz

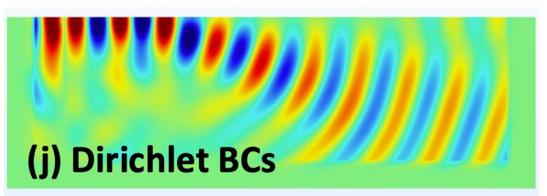
(j) Dirichlet BCs

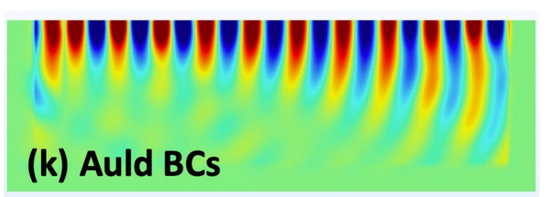
(k) Auld BCs

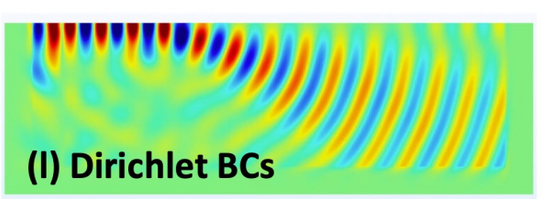
(l) Dirichlet BCs

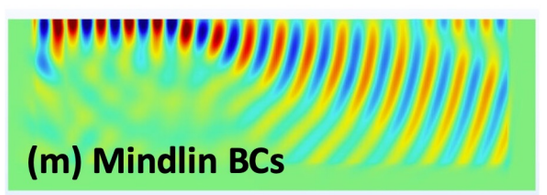
(m) Mindlin BCs

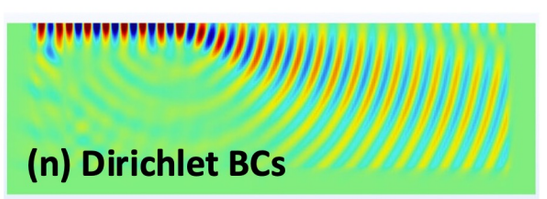
(n) Dirichlet BCs

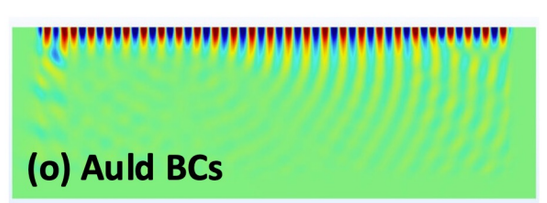
(o) Auld BCs

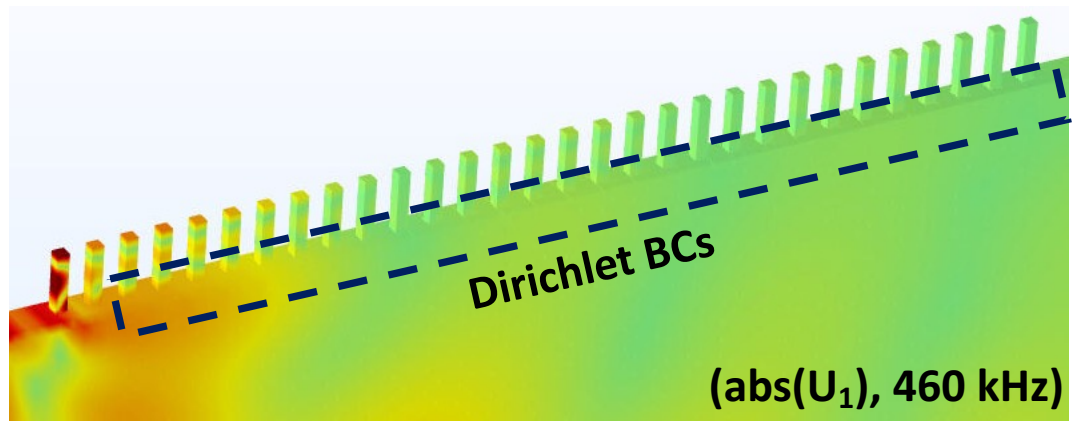

(a)

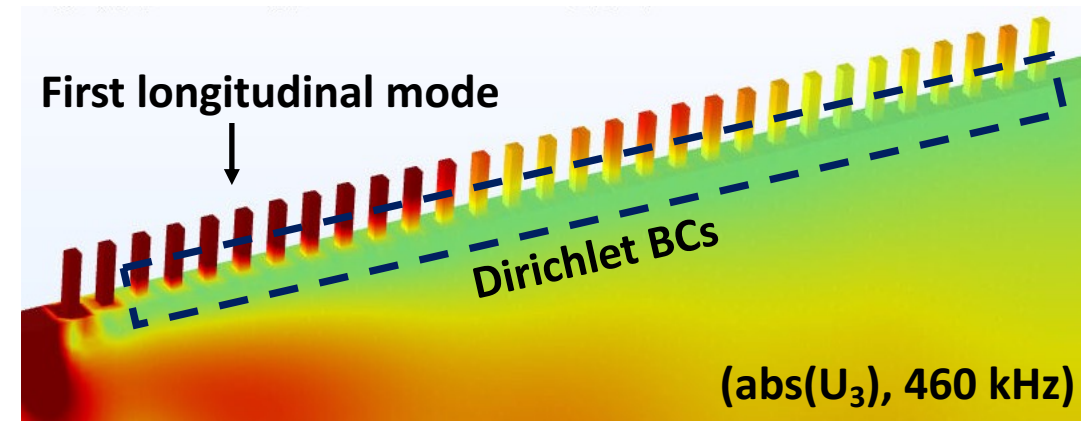

(b)

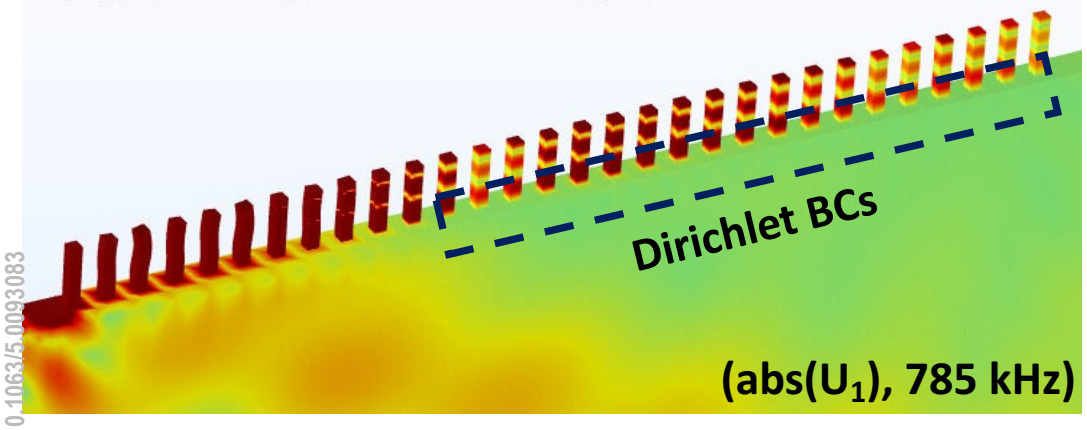

(c)

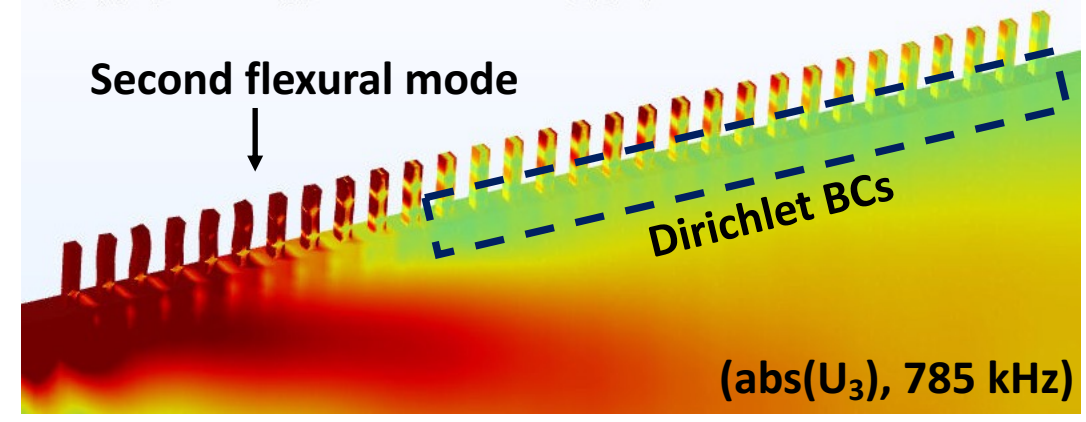

(d)

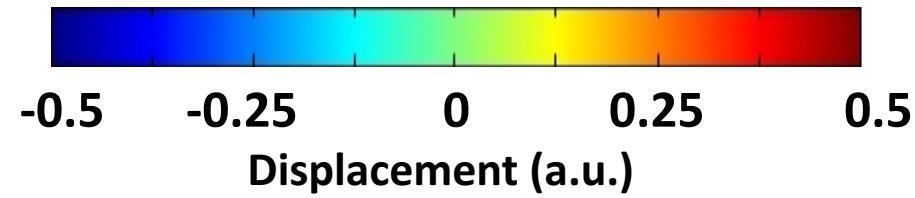

Journal of Applied Physics

AIP Publishing

AIP Publishing

Journal of Applied Physics

ACCEPTED MANUSCRIPT

PLEASE CITE THIS ARTICLE AS DOI: 10.1063/5.0093083

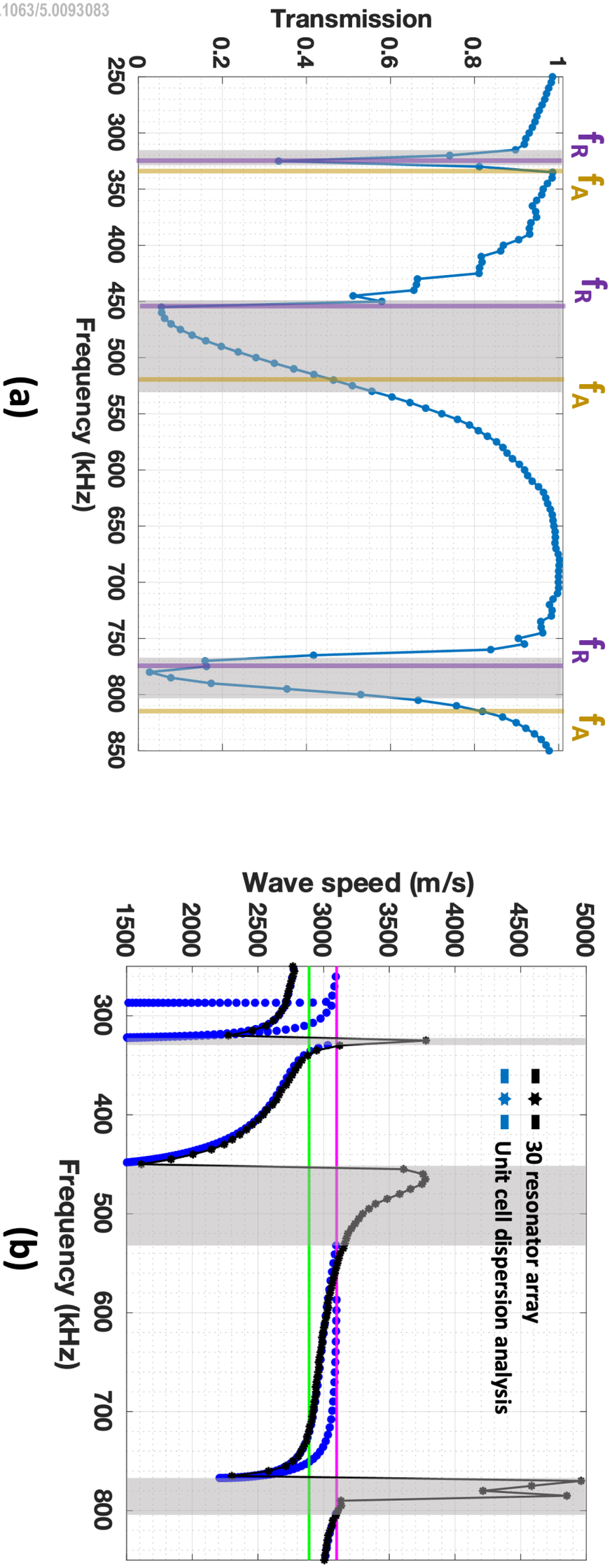

Journal of Applied Physics

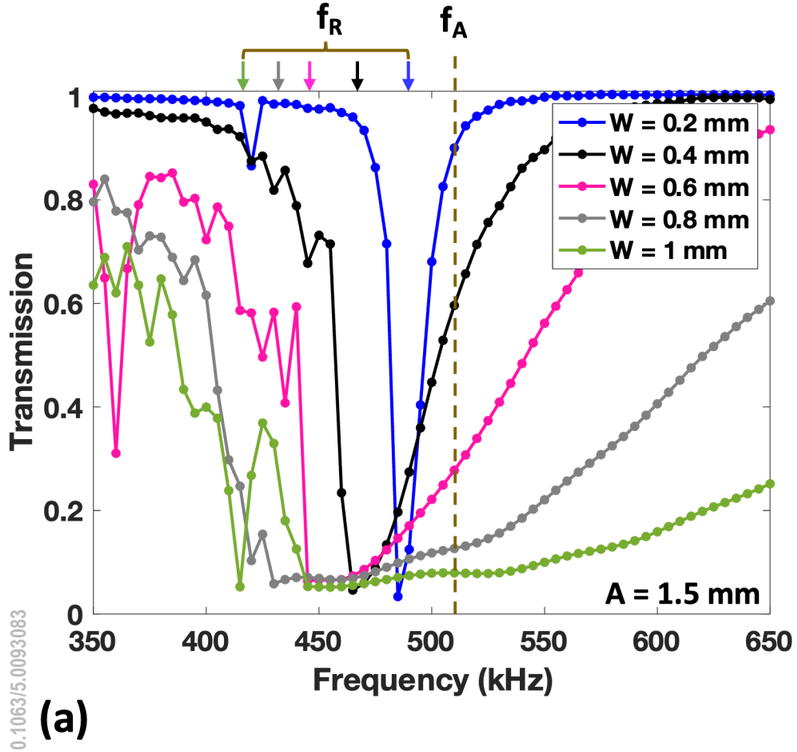

(a)

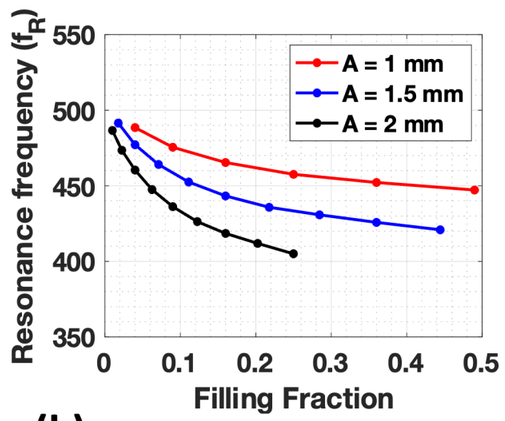

(b)

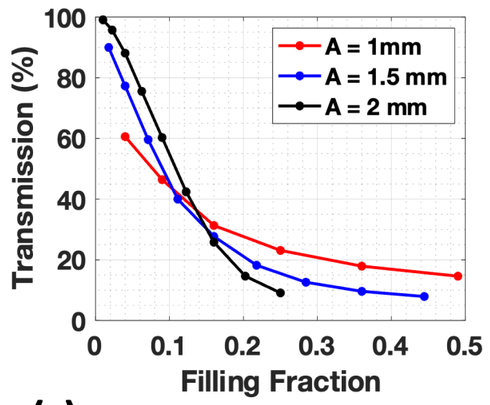

(c)

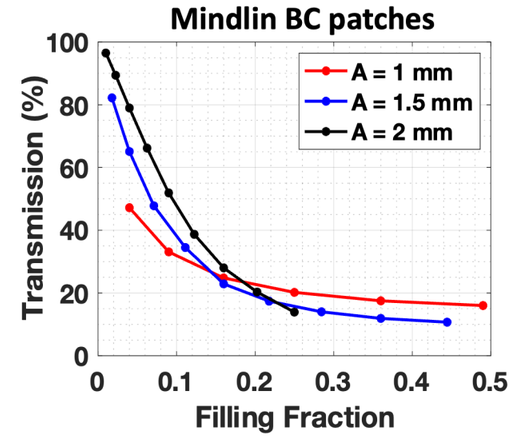

(d)

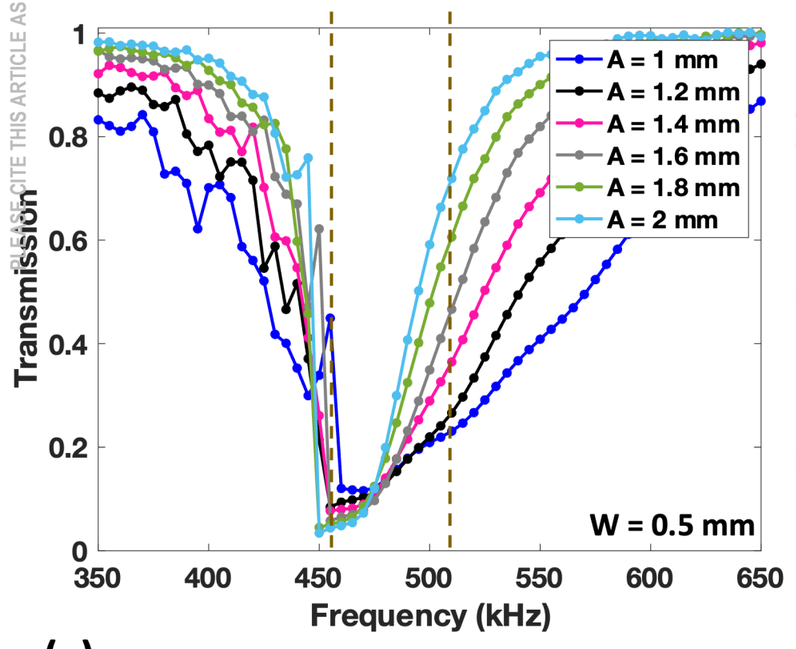

(e)

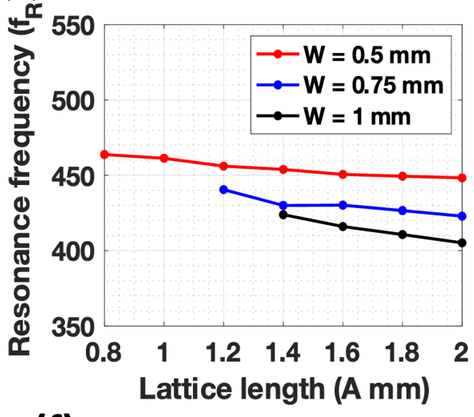

(f)

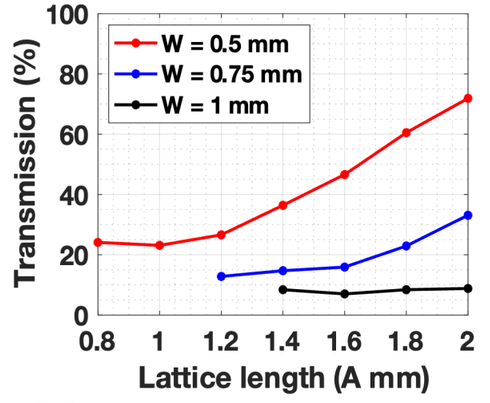

(g)

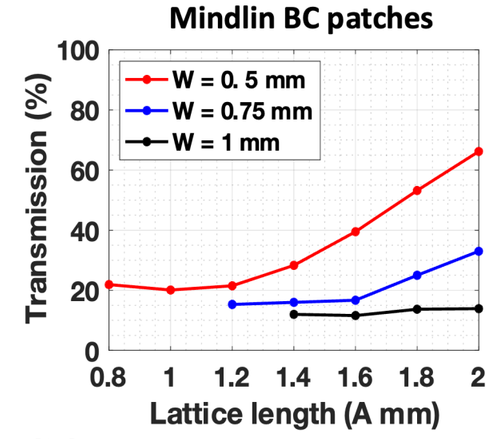

(h)